Supporting Information

Visible Lithiation Gradients of Bulk MoS_2 in Lithium-ion Coin Cells

Authors: Alexandar D. Marinov[a,b], Ami R. Shah[a], Christopher A. Howard[c], and Patrick L. Cullen‡[d]

a. Electrochemical Innovations Laboratory (EIL), Department of Chemical Engineering, University College London, WC1E 6BT, London, UK
b. CIC EnergiGUNE, Basque Research and Technology Alliance (BRTA), Alava Technology Park, Albert Einstein 48, 01510, Vitoria-Gasteiz, Spain
c. Department of Physics & Astronomy, University College London, WC1E 6BT, London, UK
d. School of Engineering and Materials Science, Queen Mary University, E1 4NS, London, UK

‡ Corresponding author(s)

Table SI 1. Ex situ cell active material mass loading, coating thickness, cycling voltage range, and state of cell disassembly.

Cell	Potential Range (V), Discharge/Charge Cycle End	Mass (mg/cm^2)	Thickness (µm)
EX1-M1	3.00 – 0.80 (**D1**)	3.69	
EX1-M2	3.00 – 0.40 (**D1**)	3.17	
EX1-M3	3.00 – 0.01 (**D1**)	3.39	
EX1-M4	3.00 – 0.01 (**C1**)	3.48	
EX2-M1	3.00 – 0.80 (**D1**)	7.48	97.2
EX2-M2	3.00 – 0.40 (**D1**)	7.75	82.2
EX2-M3	3.00 – 0.01 (**D1**)	8.60	100.2
EX2-M4	3.00 – 0.01 (**C1**)	8.32	87.2
EX3-M1	3.00 – 0.80 (**D1**)	1.27	12.9
EX3-M2	3.00 – 0.40 (**D1**)	1.54	13.9
EX3-M3	3.00 – 0.01 (**D1**)	0.97	9.9
EX3-M4	3.00 – 0.01 (**C1**)	0.76	7.4
EX4-M1	3.00 – 0.01 (**D11**)	3.55	
EX4-M2	3.00 – 0.01 (**D51**)	2.90	

Table SI 2. MoS_2 literature electrode materials, composition, source, particle size, and applied experimental current density. *Current density calculated using the areal density (mA/cm^2) or C-rate provided in the literature source and our active material loading of 3.43 mg/cm^2.

Active Material	Composition (Active:Conductive: Binder)	Prod. Identifier	Particle Size (µm)	Current Density (mA/g)	Ref.
Commercial MoS_2	80:10:10	>99% Alfa	-	35	1
Commercial MoS_2	80:10:10	>99% Alfa	-	29*	2
Commercial MoS_2	80:10:10	Alfa 98 %	-	100	3
Commercial MoS_2	80:10:10	Sigma Prod. No. 234842	< 2 µm	100 – 200	4
Commercial MoS_2	80:10:10	Sigma. Prod. No. 69860	~ 6 µm	100	5
Commercial MoS_2	80:10:10	Sigma	~ 6 µm	50	6
Commercial MoS_2	70:20:10	-	-	200	7
Commercial MoS_2	70:20:10	Macklin 99%	< 2 µm	84*	8

As-cast Electrode Characterisation

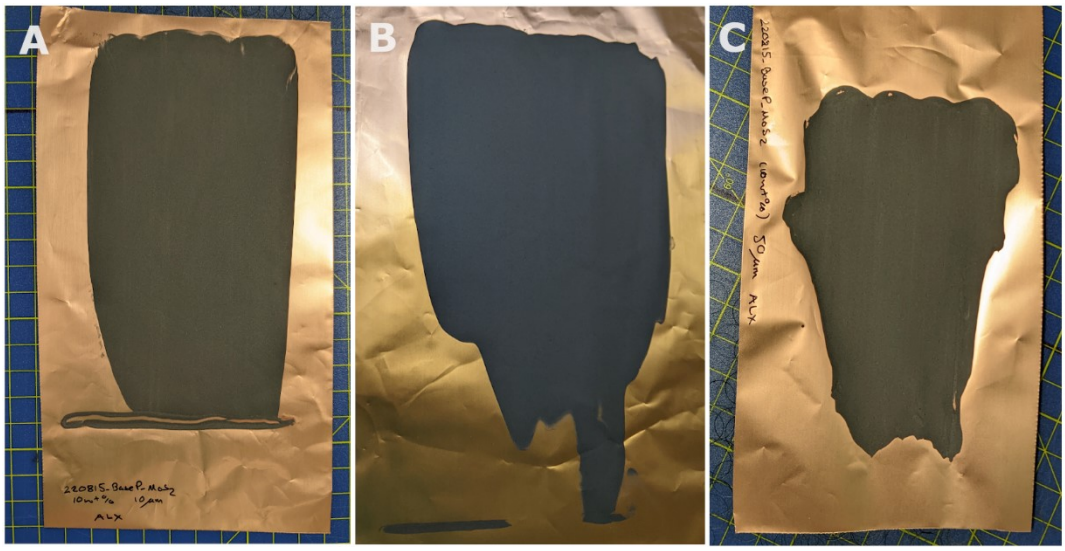

Figure SI 1. Battery electrodes with composition 80:10:10 wt. % of MoS_2, carbon Super P, and PVDF binder on a copper substrate (11 µm thick). Average electrode coating thickness (A) ~ 12 µm, (B) ~ 36 µm, and (C) ~ 89 µm.

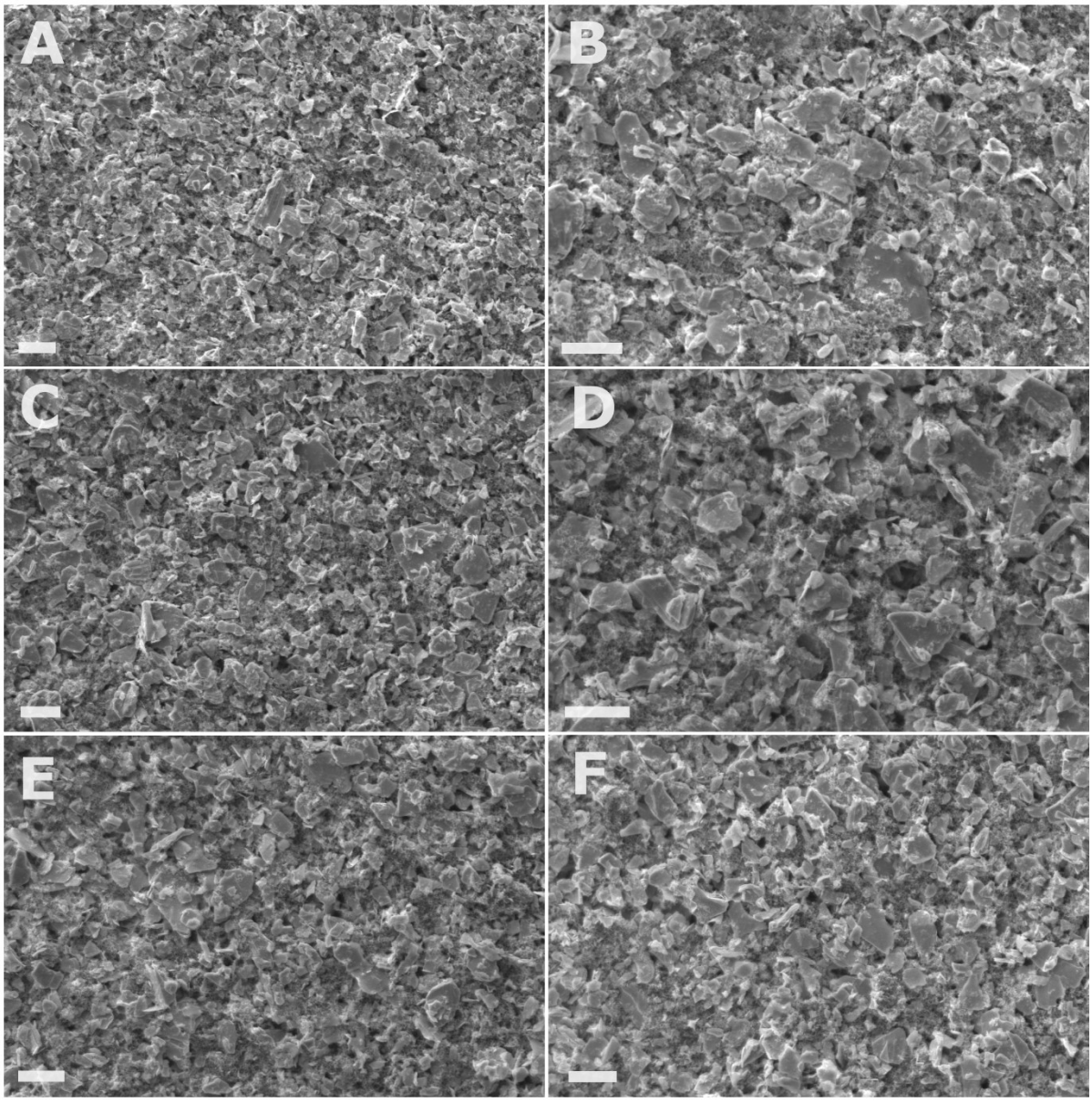

Figure SI 2. SEM of the pristine MoS_2 battery electrodes used in the study (A, B) ~ 12 µm, (C, D) ~ 36 µm, and (E, F) ~ 89 µm. All scale bars 10 µm.

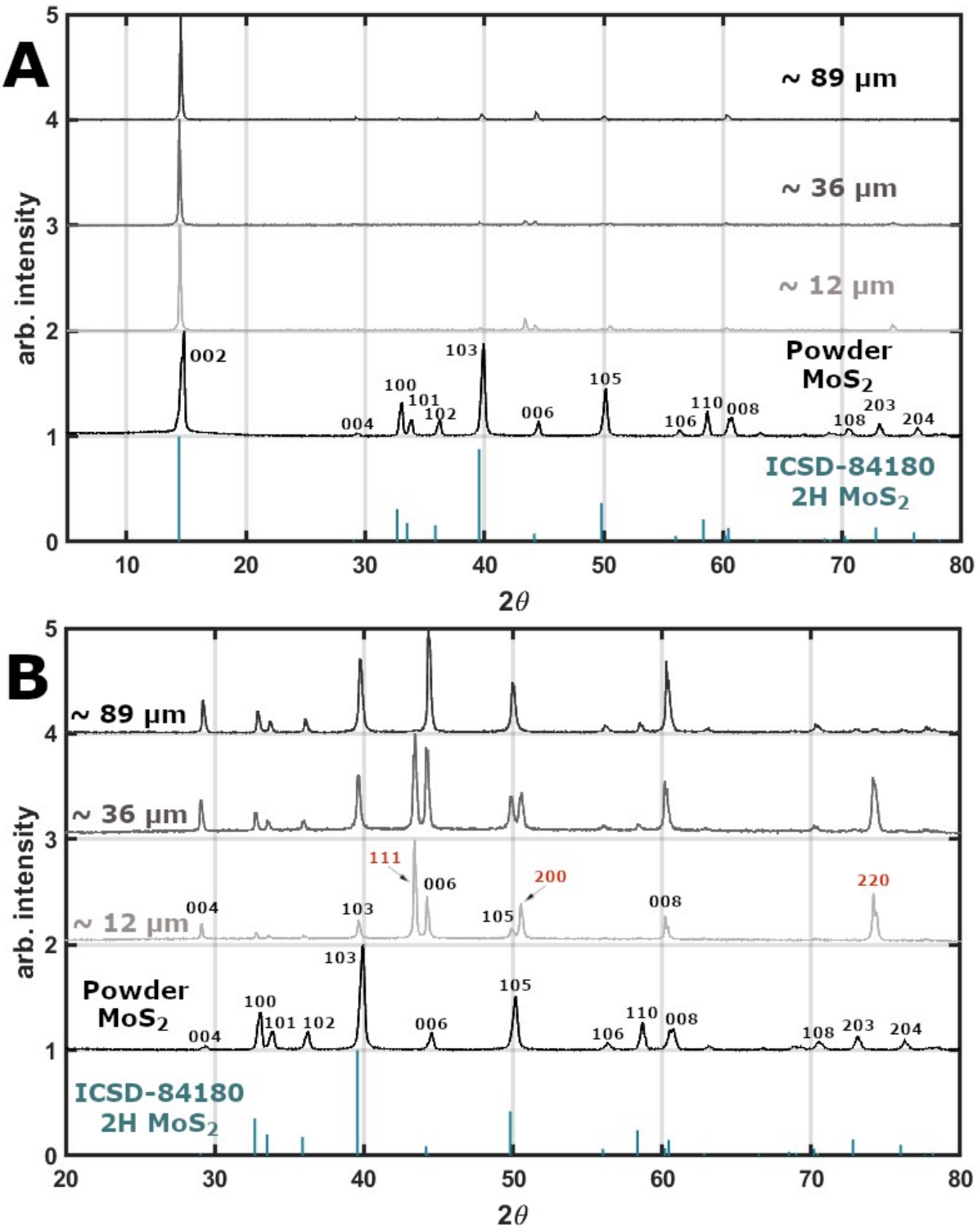

Figure SI 3. XRD (Cu source) of the pristine MoS_2 battery electrodes used in the study. Values normalised relative to the highest intensity in the diffraction pattern. Black indices belong to ICSD-84180 MoS_2 and red indices belong to the copper current collector.

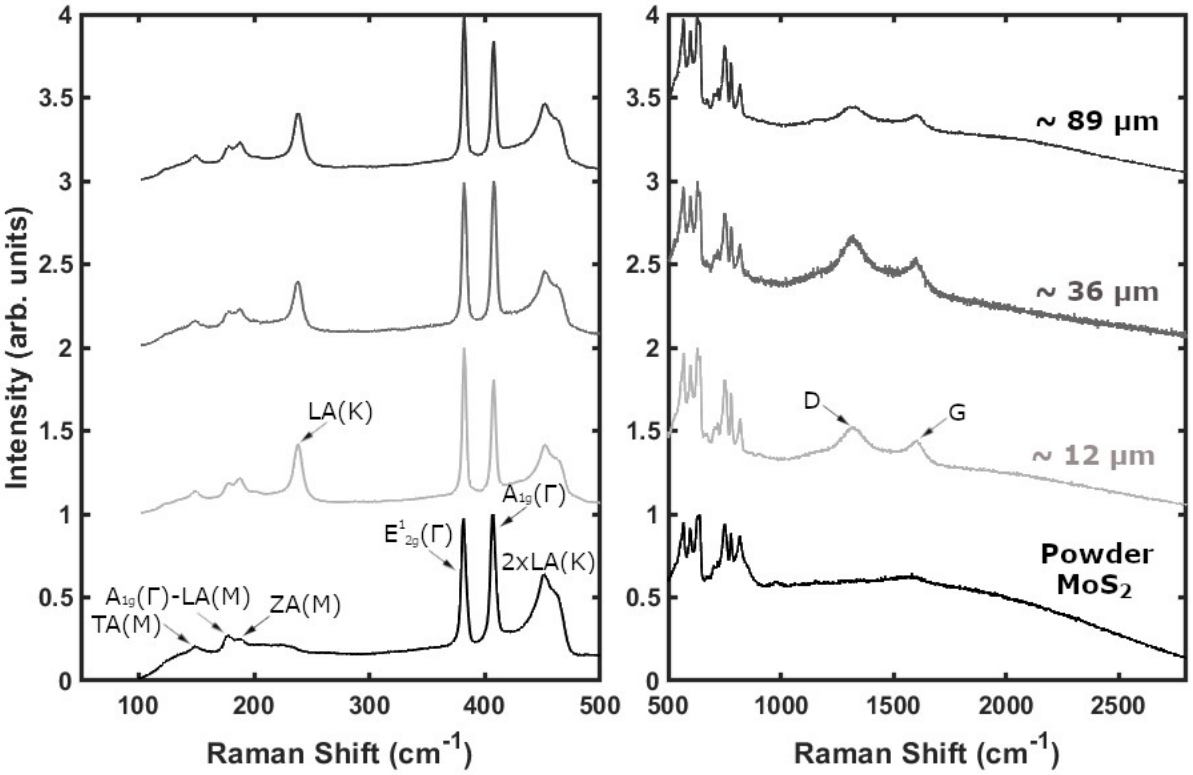

Figure SI 4. Raman spectroscopy (785 nm laser) of the pristine MoS_2 battery electrodes used in the study. Data normalised relative to the highest value in each spectrum.

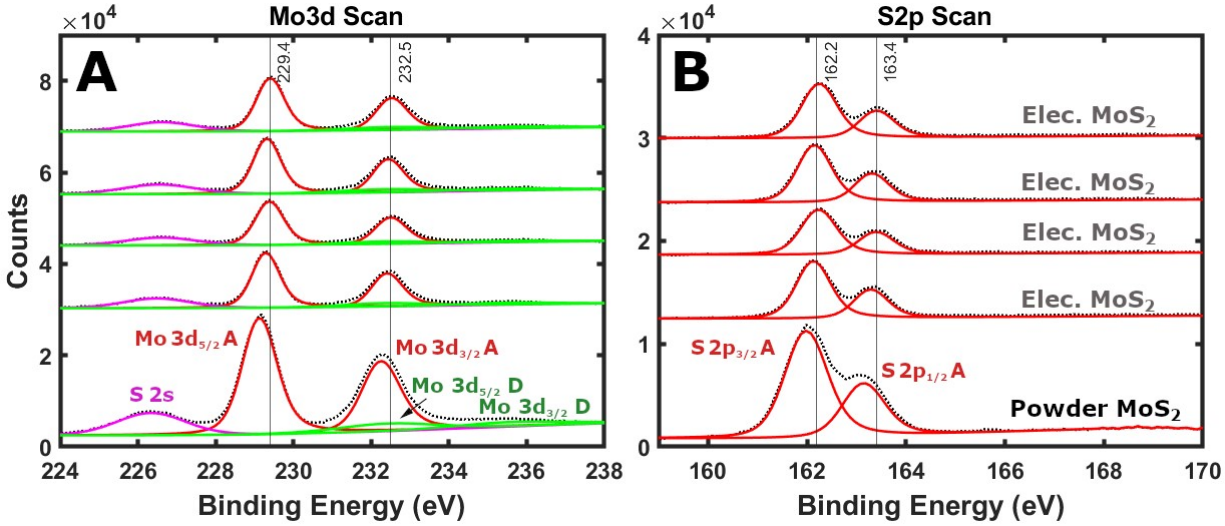

Figure SI 5. XPS of pristine MoS_2 powder used to make electrode and the MoS_2 battery electrode (~ 36 µm) used in the study. Four points scanned for consistency. (A) Mo 3d and (B) S 2p XPS regions.

Table SI 3. Thickness measurements of 15 mm diameter electrodes used throughout the study.

Electrode	Number Discs Sampled	STD Thickness (µm)	Avg. Thickness (µm)
~12 µm	12	± 2.7	11.5
~36 µm	25	± 4.6	35.8
~89 µm	8	± 5.8	89.1

Table SI 4. Active mass measurements of 15 mm diameter electrodes used throughout the study.

Electrode	Number Discs Sampled	STD Active Mass (mg)	Avg. Active Mass (mg)	Avg. Active Mass Loading (mg/cm^2)
~12 µm	10	± 0.53	1.96	1.11
~36 µm	12	± 0.39	6.06	3.43
~89 µm	10	± 0.55	14.40	8.15

Electrochemical Data

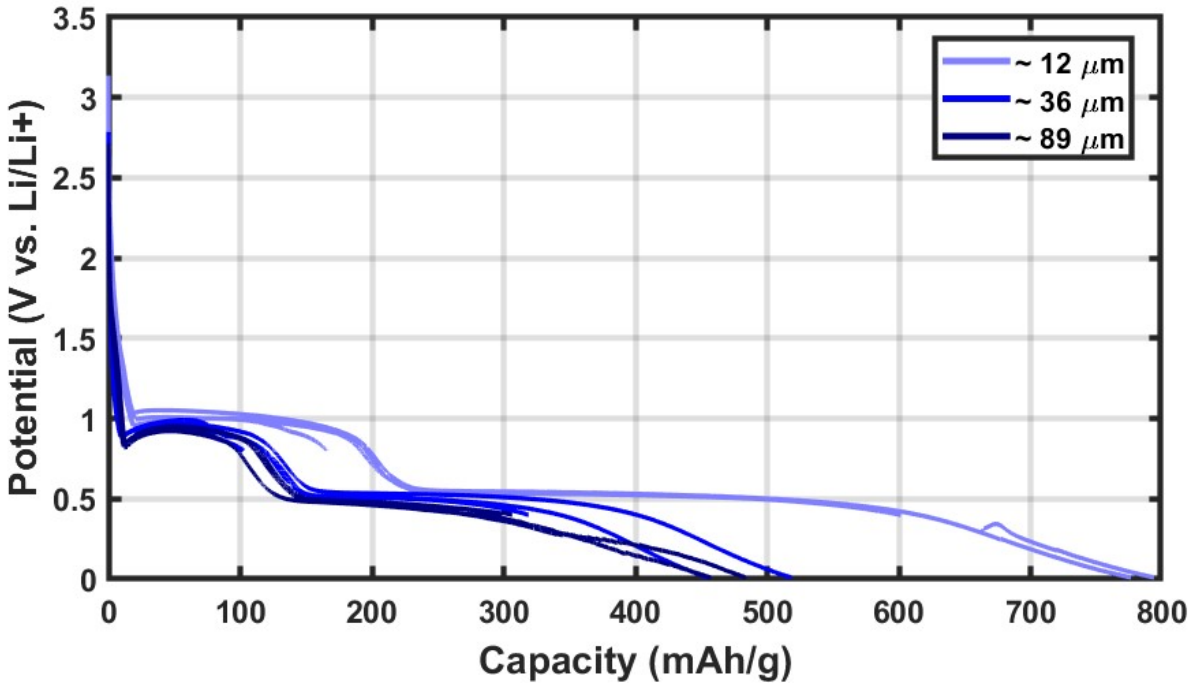

Figure SI 6. Specific capacity for the first discharge (lithiation) of MoS_2 electrodes of thickness ~ 12 µm, ~ 36 µm, and ~ 89 µm with voltage cutoffs **D1 0.80 V**, **D1 0.40 V**, **D1 0.01 V**, and **C1 3.00 V**.

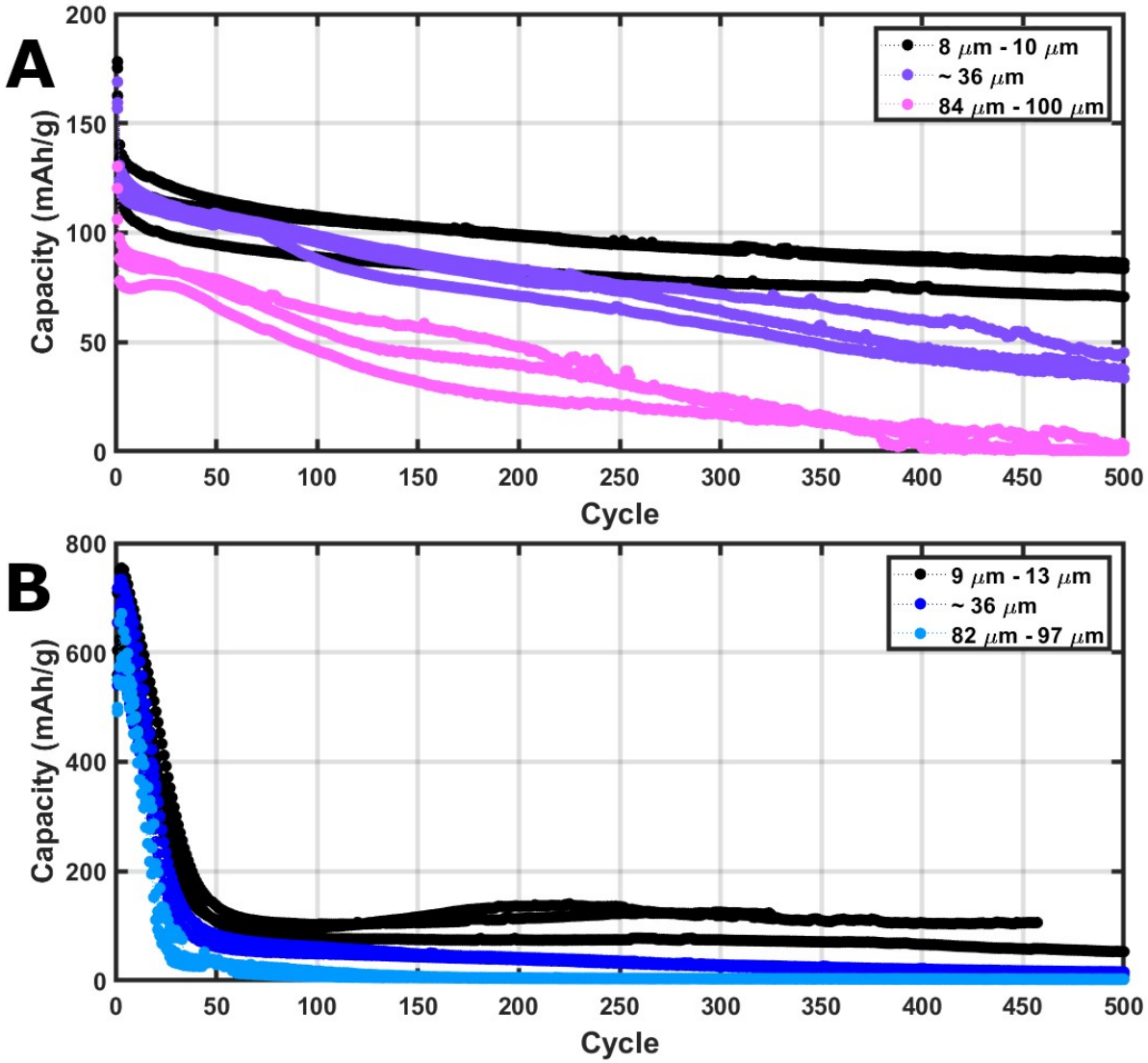

Figure SI 7. Discharge capacity plots of MoS_2 electrodes of varying thickness cycled at a constant current density of 100 mA/g versus a Li metal counter electrode, within voltage ranges of (A) 3.00 – 0.80 V and (B) 3.00 – 0.01 V.

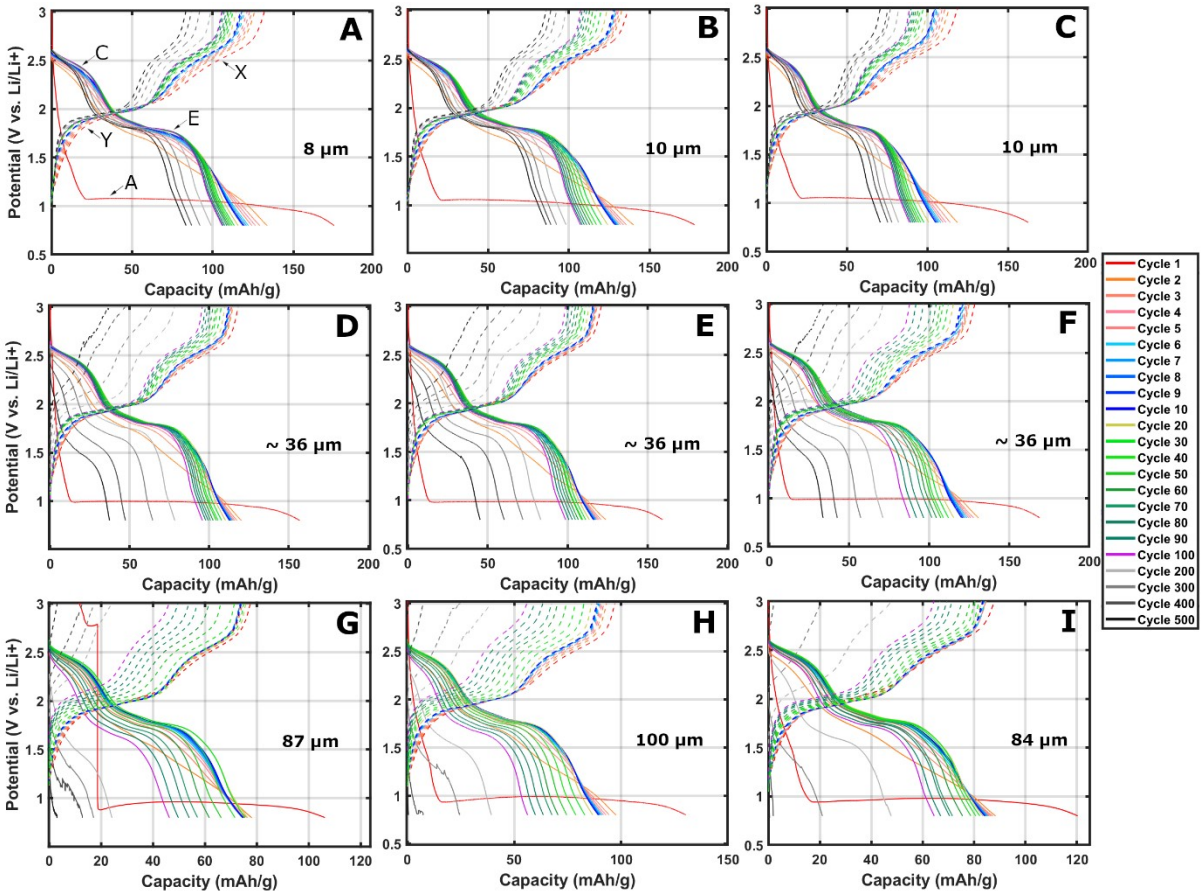

Figure SI 8. Voltage profiles of MoS_2 electrodes of varying thickness cycled at a constant current density of 100 mA/g versus a Li metal counter electrode, within a shallow discharge (3.00 – 0.80 V) voltage range.

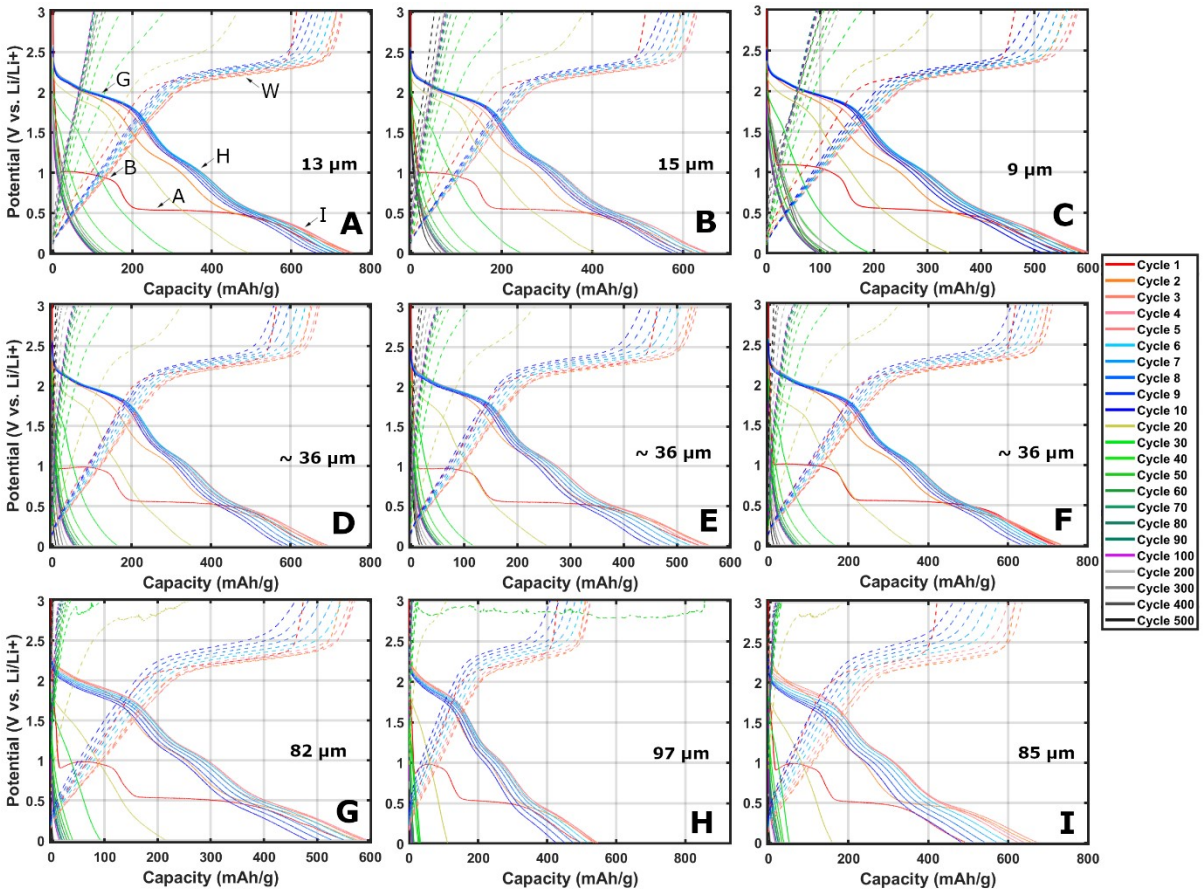

Figure SI 9. Voltage profiles of MoS_2 electrodes of varying thickness cycled at a constant current density of 100 mA/g versus a Li metal counter electrode, within a deep discharge (3.00 – 0.01 V) voltage range.

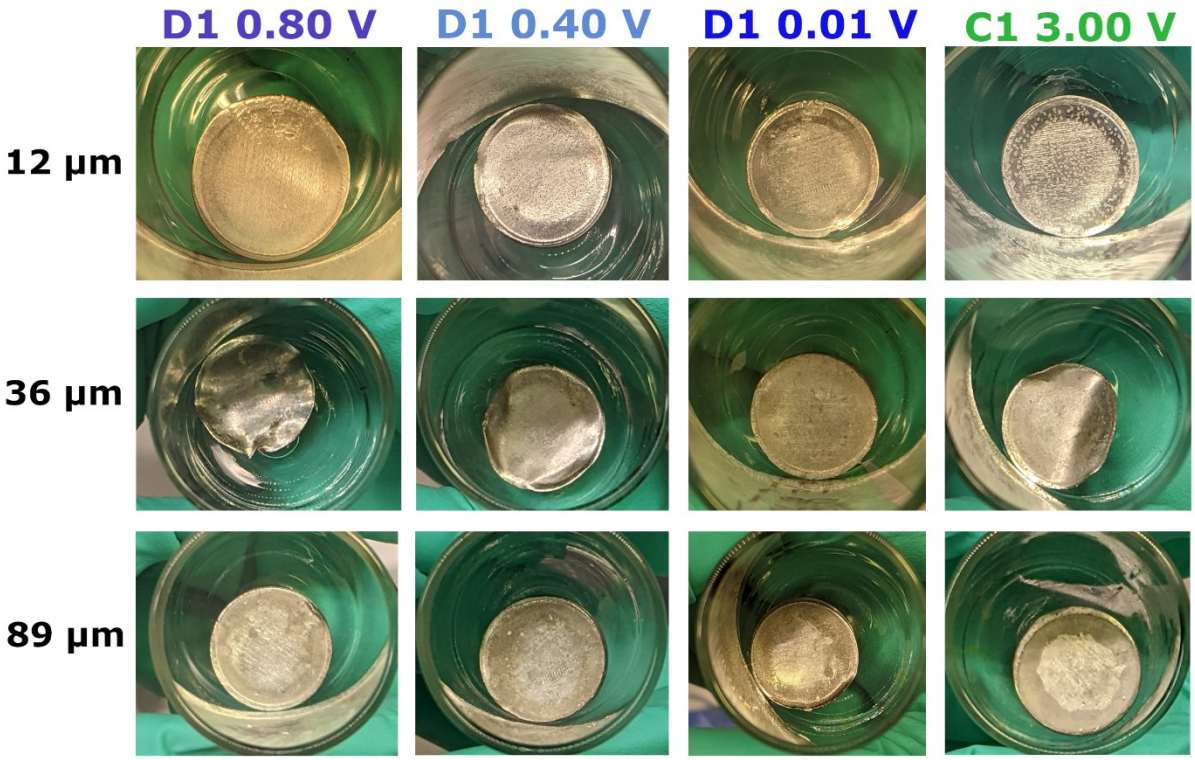

Ex situ MoS_2 LIB Electrode Characterisation

Figure SI 10. Digital images of the cycled lithium metal counter electrodes to the MoS_2 electrodes shown in Figure 2. The denoted thickness is for the MoS_2 working electrodes and not the lithium counters.

Figure SI 11. Digital images of (A) pristine lithium metal foil, (B – G) ~ 89 µm thick cycled MoS_2 ex situ working electrodes and their corresponding lithium counter electrodes. (B, C) **D1 0.40 V**, (D, E) **D1 0.01 V**, and (F, G) **C1 3.00 V**.

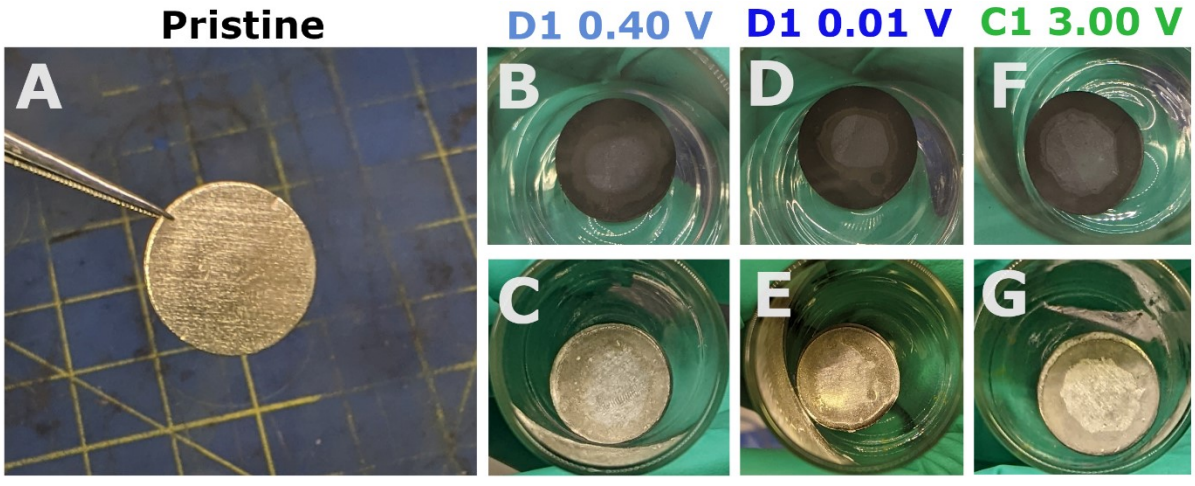

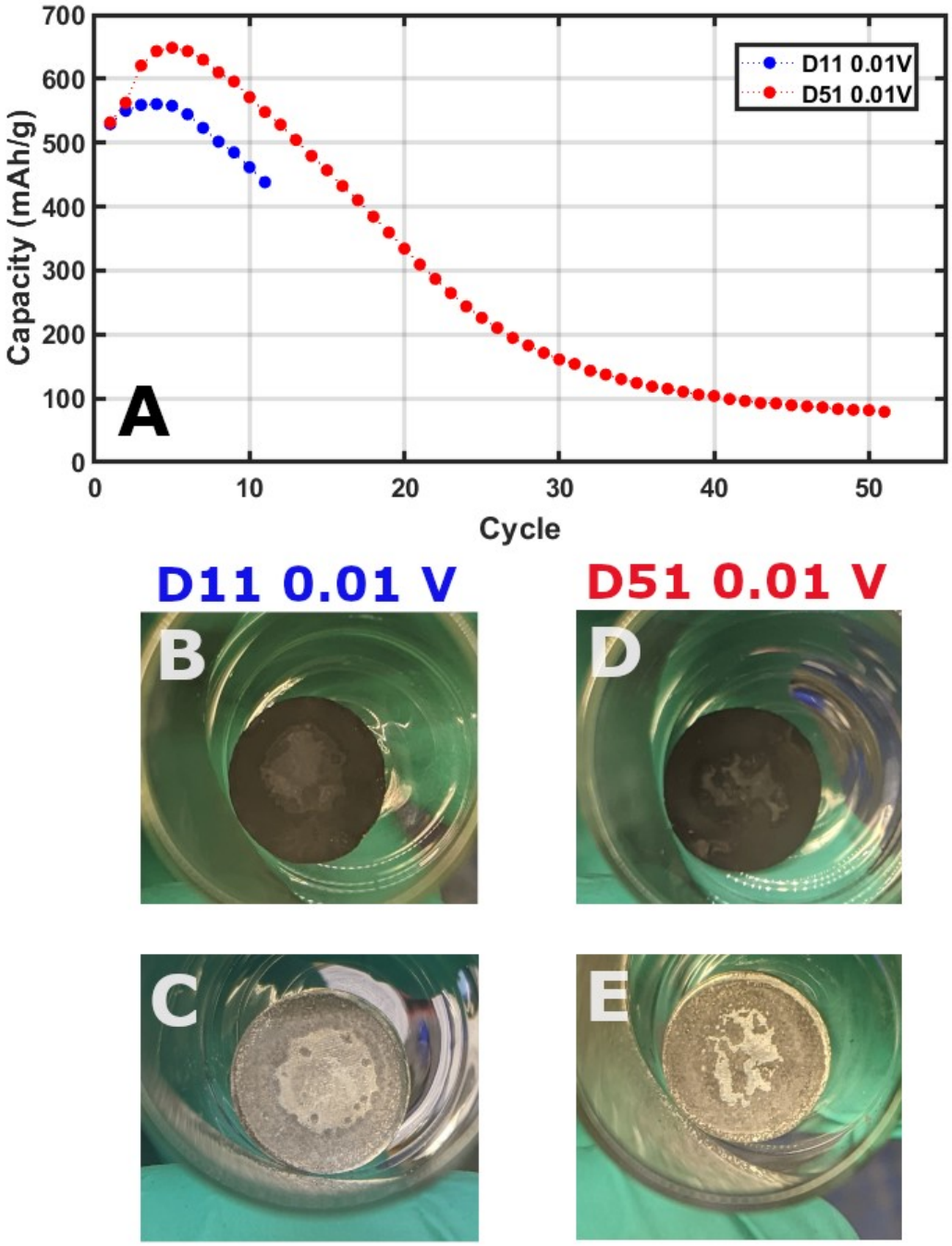

Figure SI 12. Ex situ long-term MoS_2 electrodes (~ 36 µm) cycled at 100 mA/g in lithium counter LIB cells.

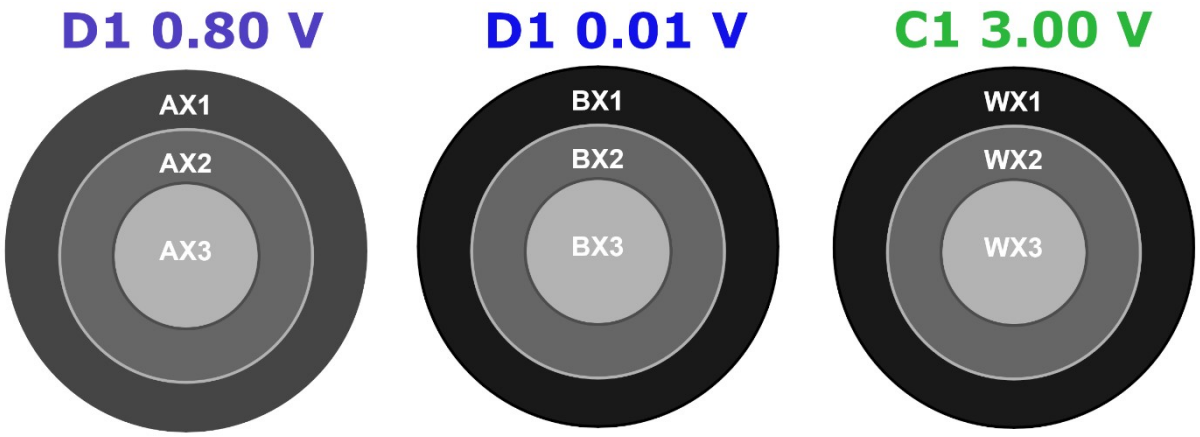

Figure SI 13. Nomenclature for the different coloured rings in the first cycle of MoS_2 LIB operation for the ~ 36 µm thick electrodes.

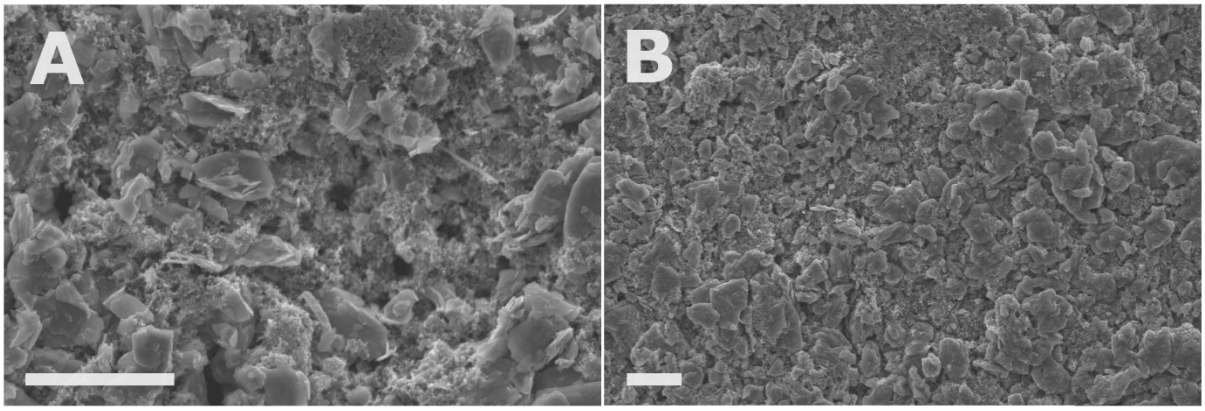

Figure SI 14. Ex situ SEM of **D1 0.01 V** ~ 36 µm electrode middle ring (**BX2**). Scale bars are 10 µm.

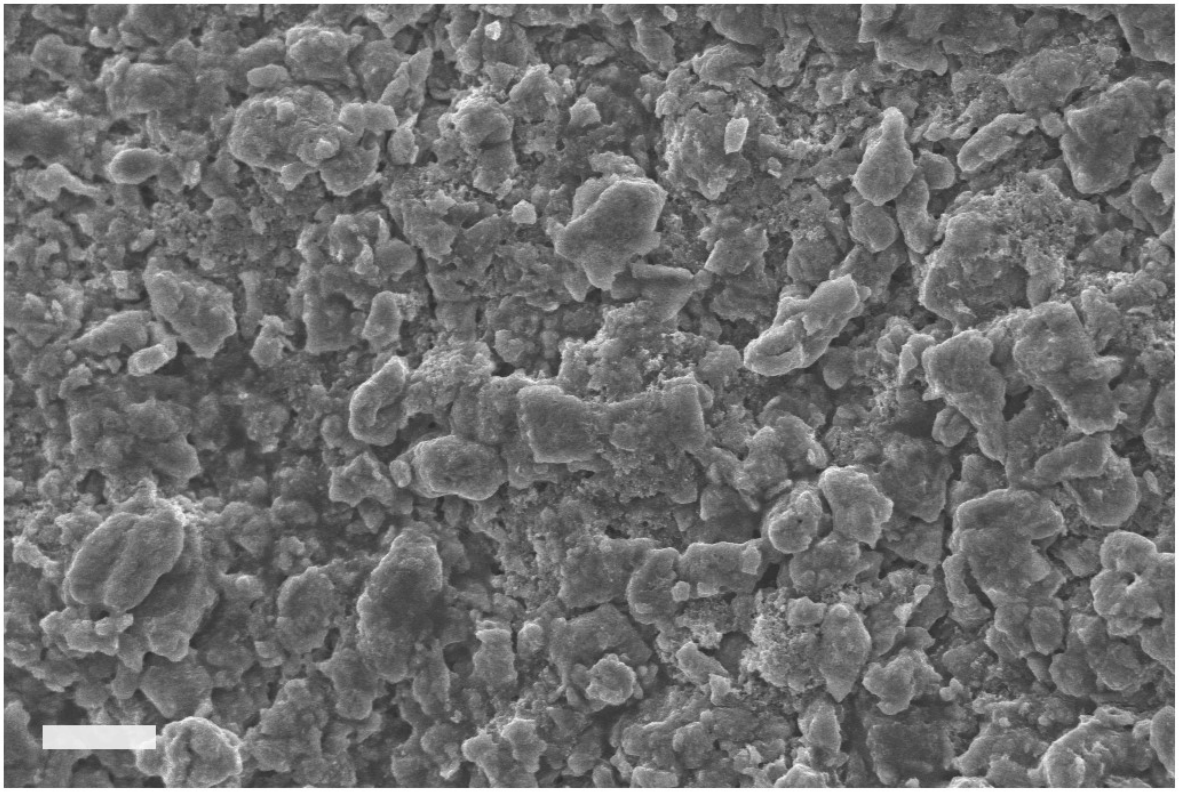

Figure SI 15. Ex situ SEM of **D1 0.01 V** ~ 36 µm electrode outer ring (**BX1**). Scale bar is 10 µm.

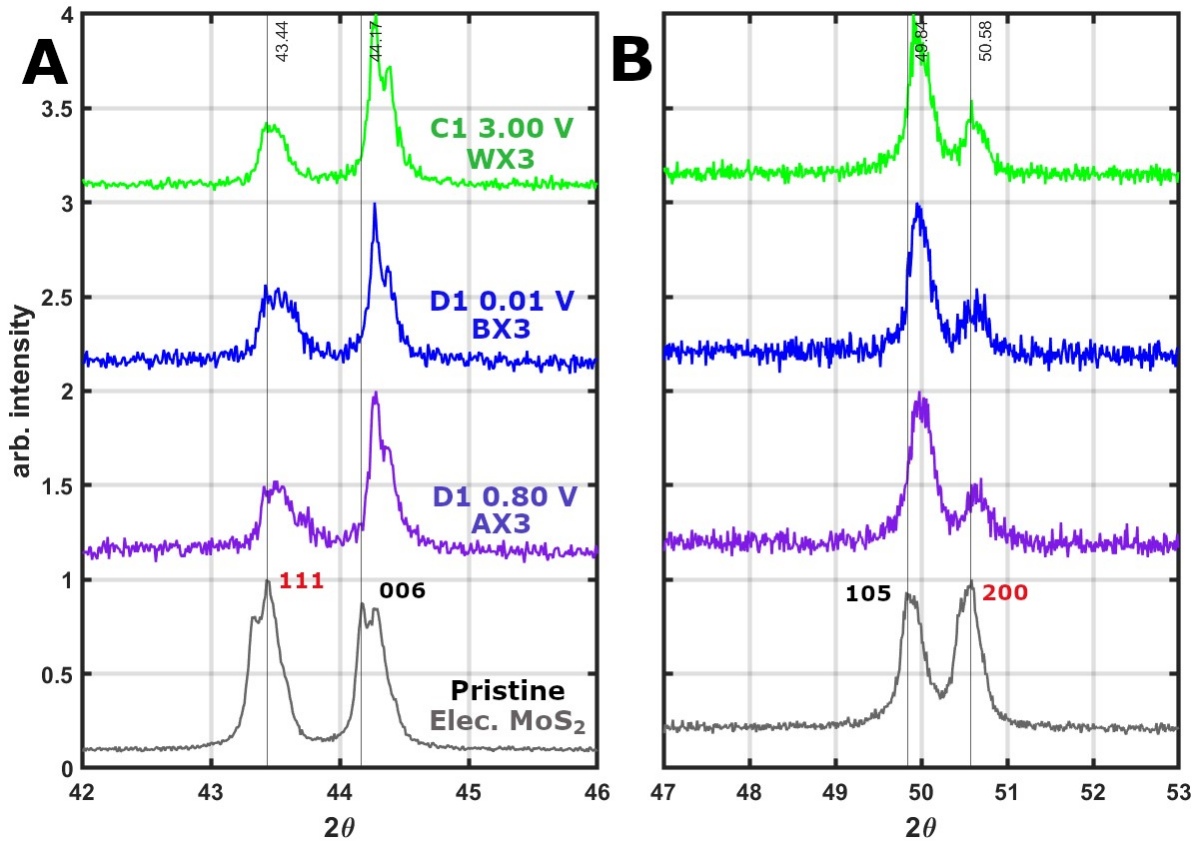

Figure SI 16. Ex situ XRD (Cu source) of the **central rings** of ~ 36 µm thick MoS_2 electrodes cycled to **D1 0.80 V** (**AX3**), **D1 0.01 V** (**BX3**), and **C1 3.00 V** (**WX3**) in a lithium-metal half-cell at a current density of 200 mA/g. Black indices denote MoS_2 and the red indices belong the to the Cu current collector.

The ex situ cycled samples experience an upshift in 2θ values relative to the pristine electrode (Figure SI 16). However, the cycled samples have carbon tape underneath them, raising their height relative to the pristine electrode. Therefore, it is necessary to validate whether the upshift in 2θ is caused by the LIB process or simply by the height difference.

Since, the copper current collector indices are not affected by lithiation, their upshift by the same value as the MoS_2 indices relative to the pristine electrode, signifies that the 2θ shift is caused by the addition of carbon tape beneath the sample.

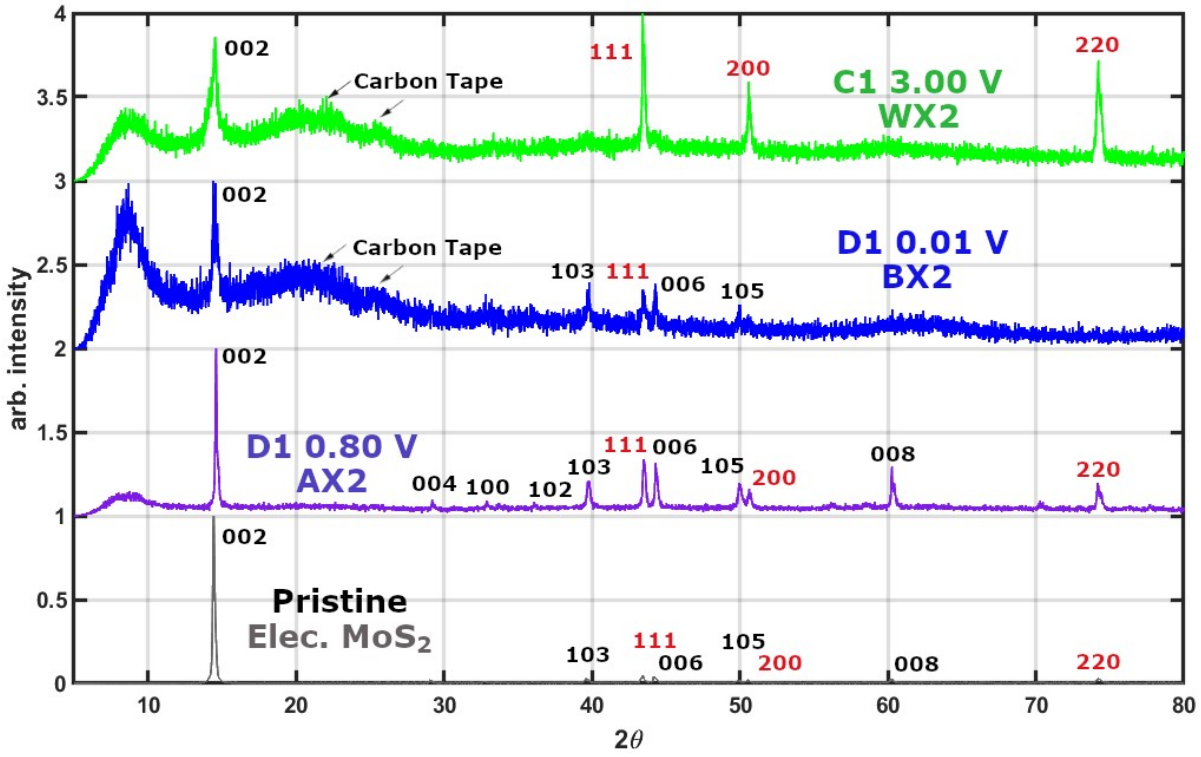

Figure SI 17. Ex situ XRD (Cu source) of the **middle rings** of ~ 36 µm thick MoS_2 electrodes cycled to **D1 0.80 V** (**AX2**), **D1 0.01 V** (**BX2**), and **C1 3.00 V** (**WX2**) in a lithium-metal half-cell at a current density of 200 mA/g.

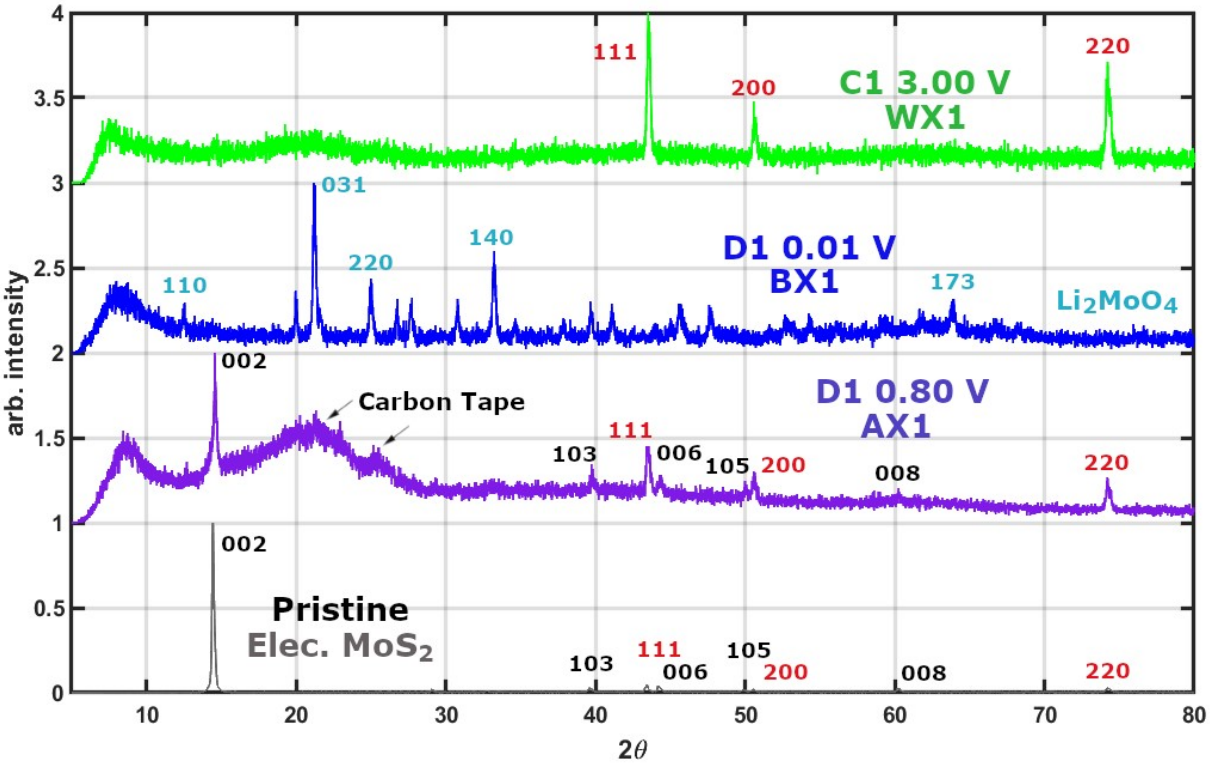

Figure SI 18. Ex situ XRD (Cu source) of the **outer rings** of ~ 36 µm thick MoS_2 electrodes cycled to **D1 0.80 V** (**AX1**), **D1 0.01 V** (**BX1**), and **C1 3.00 V** (**WX1**) in a lithium-metal half-cell at a current density of 200 mA/g.

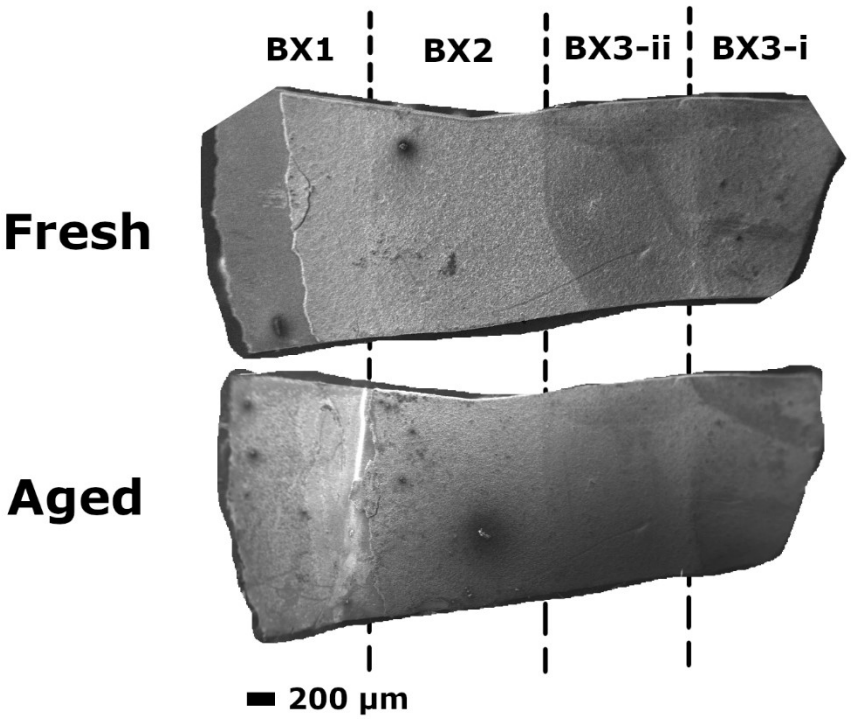

Figure SI 19. Ex situ SEM of **D1 0.01 V** (~ 47 µm) electrode segment fresh (1 month) and aged in air (12 months).

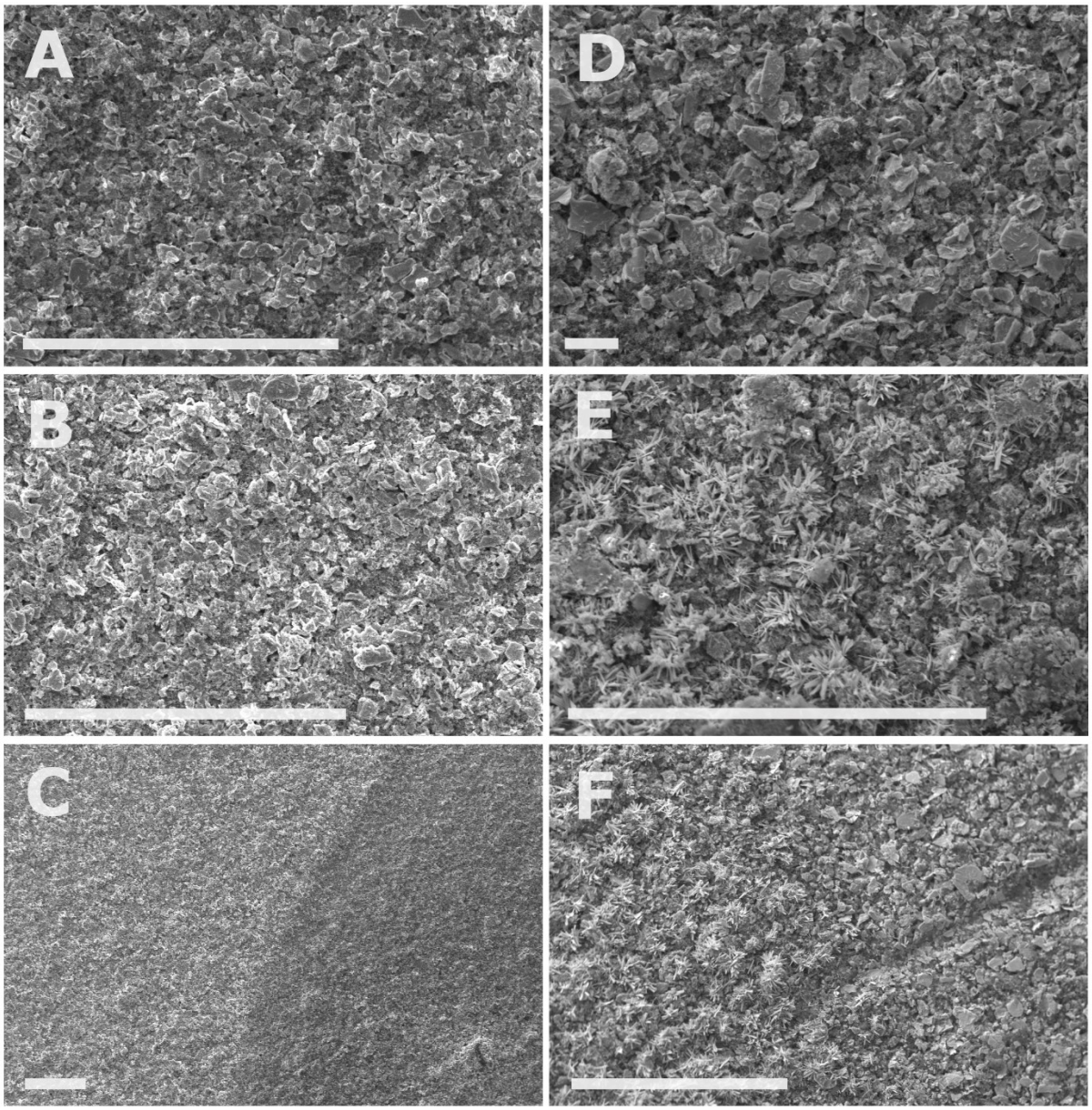

Figure SI 20. Ex situ SEM of **D1 0.01 V** electrode segment (~ 47 µm). Images taken after 1 month of air exposure: (A) **BX3-i**, (B) **BX2**, and (C) **BX2/BX3-ii** border. Images taken 12 months after air exposure: (D) **BX3-ii**, (E) **BX2**, and (F) **BX2/BX3-ii** border. Scale bars are 10 µm in D and 100 µm in the rest.

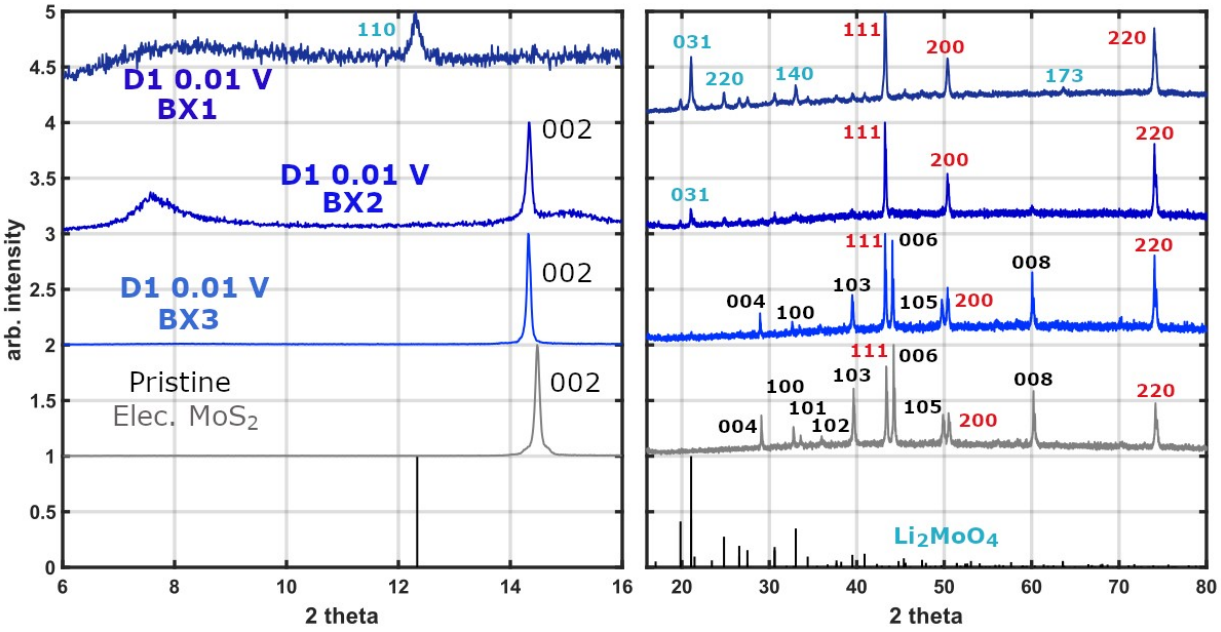

Figure SI 21. Ex situ XRD (Cu source) of **D1 0.01 V** cell (~ 47 µm) aged in air for 5 months.

Note I: Ageing of a Lithiated MoS_2 Electrode in Air

To consider the effects of atmospheric exposure of a cycled **D1 0.01 V** electrode SEM was conducted 1 month after exposure to air and 12 months after exposure. As a direct comparison (Figure SI 19), the fresh samples included four distinct regions **BX1**, **BX2**, **BX3-i**, and **BX3-ii**. It is noted that the only difference between **BX3-i** and **BX3-ii** is the height of the sample, which might be caused by an uneven pressure distribution within the coin cell or bending during sample preparation for SEM.

With ageing, the outer most region **BX1** flakes off completely from the copper current collector. Showcasing the fragile nature of lithiated MoS_2 electrodes. This occurrence happens often with the outer most **BX1** ring. Noticeably, region **BX1** appears thinner than **BX2**; however, this is not observed in any other electrode sample and is therefore unlikely to be caused by the coin cell configuration.

Morphologically, within the fresh sample there is no difference between **BX3** and **BX2** (Figure SI 20A – B). Both areas display the usual MoS_2 flake-like structures. However, the charge build-up observed on their surface from the SEM beam is starkly different. Charge builds up strongly on **BX2**, making the boundary between the two regions easily distinguishable (Figure SI 20C).

Following 12 months of ageing in atmospheric conditions, the electrode centre **BX3** retains the MoS_2 flake-like morphology with similar charge dissipation (Figure SI 20D). On the other hand, the middle **BX2** exhibits the formation of sharp crystalline rods on the electrode surface (Figure SI 20E) and the loss of charge build-up from the flakes underneath. Again, due to their differences the **BX2** and **BX3** sections can easily be distinguished (Figure SI 20F).

Crystallographic analysis of the aged (12 months) electrode (Figure SI 21), indicates the electrode centre **BX3** to remain as 2H MoS_2, the middle ring **BX2** to contain both MoS_2 and a small amount of crystalline Li_2MoO_4, and the outer ring **BX1** to solely contain Li_2MoO_4.

Thus, it can be concluded that the lithiated species present in the middle and outer rings react slowly with oxygen when exposed to air, resulting in the gradual formation of Li_2MoO_4. However, Li_2MoO_4 itself is not present immediately following air exposure nor is it formed within the LIB cell.

Ex situ Electrode Raman Spectroscopy: Coloured Ring Section Consistency

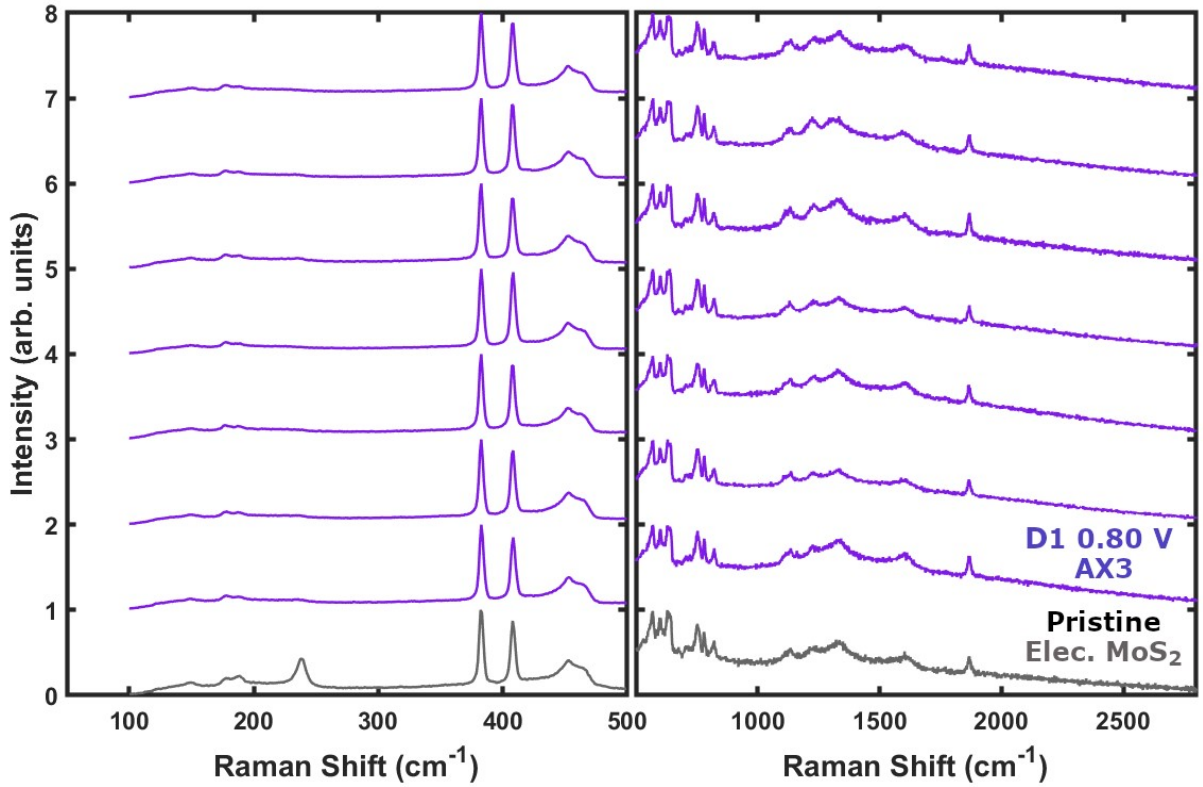

Figure SI 22. Ex situ air-free Raman spectroscopy (785 nm) of **D1 0.80 V** (~ 36 µm) electrode segment **AX3**. Multiple locations scanned across the electrode for MoS_2 phase consistency.

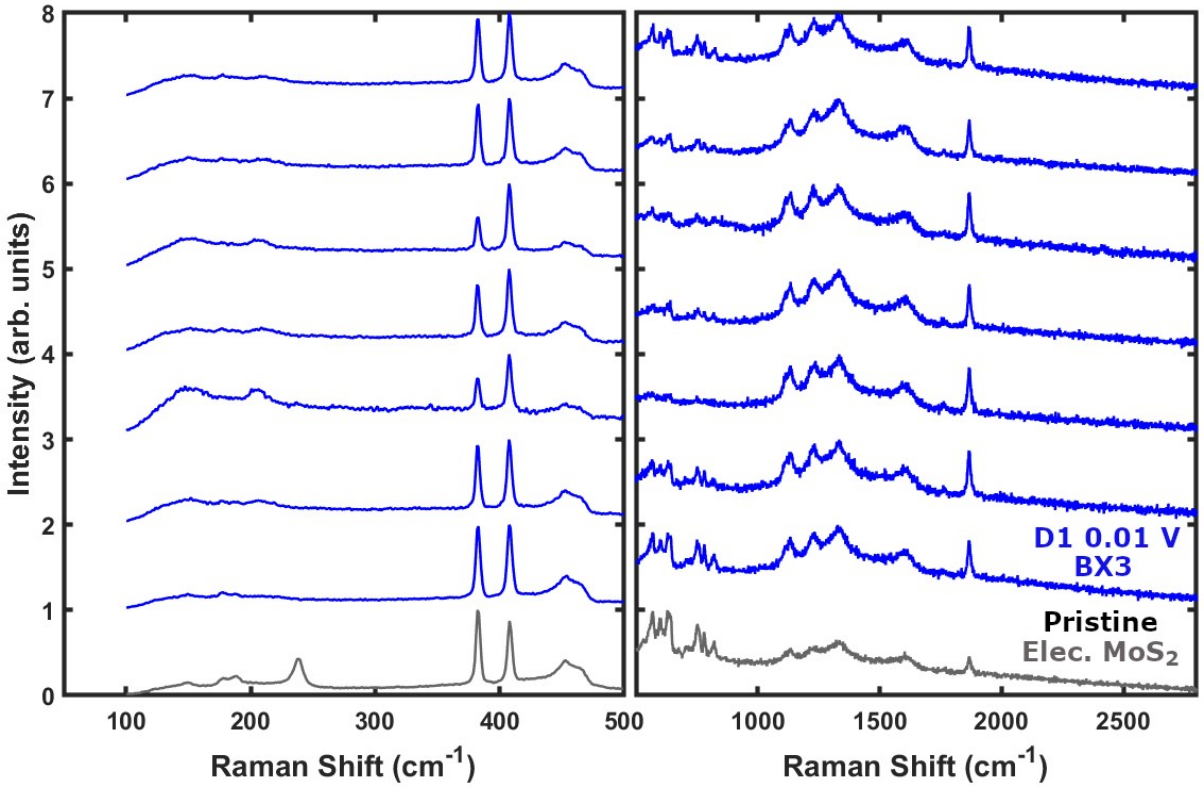

Figure SI 23. Ex situ air-free Raman spectroscopy (785 nm) of **D1 0.01 V** (~ 36 µm) electrode segment **BX3**. Multiple locations scanned across the electrode for MoS_2 phase consistency.

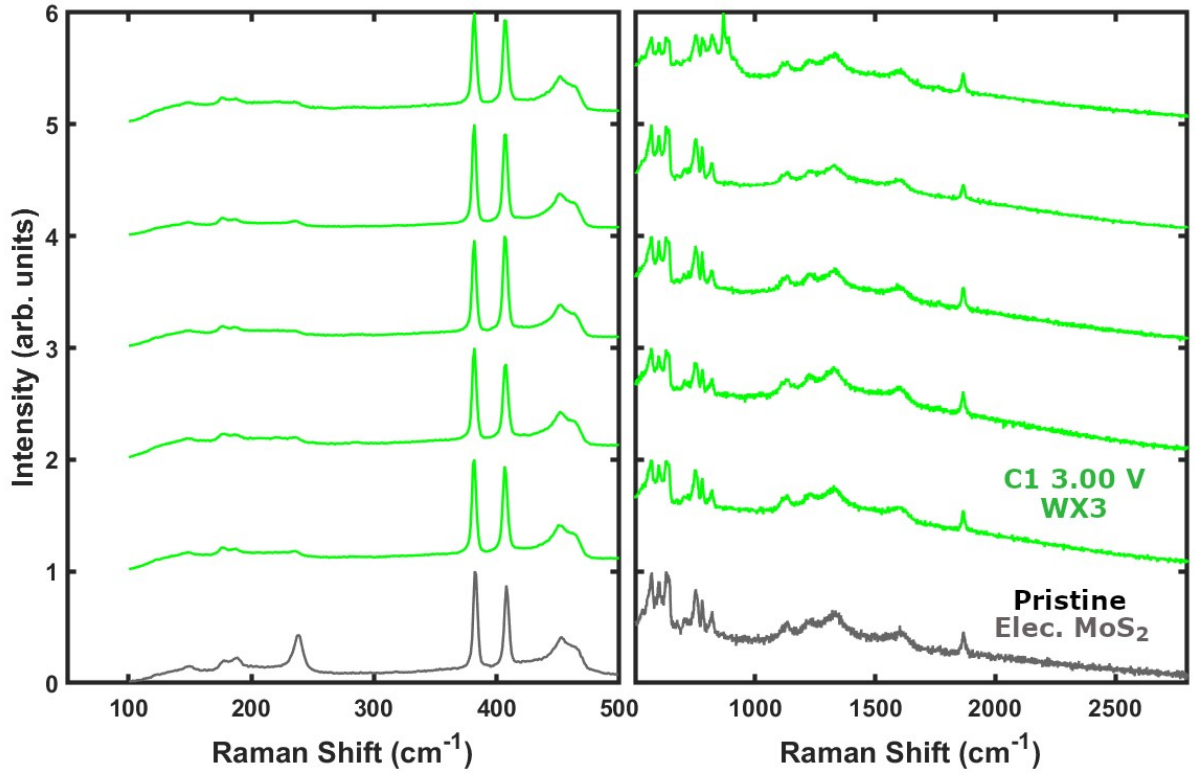

Figure SI 24. Ex situ air-free Raman spectroscopy (785 nm) of **C1 3.00 V** (~ 36 µm) electrode segment **WX3**. Multiple locations scanned across the electrode for MoS_2 phase consistency.

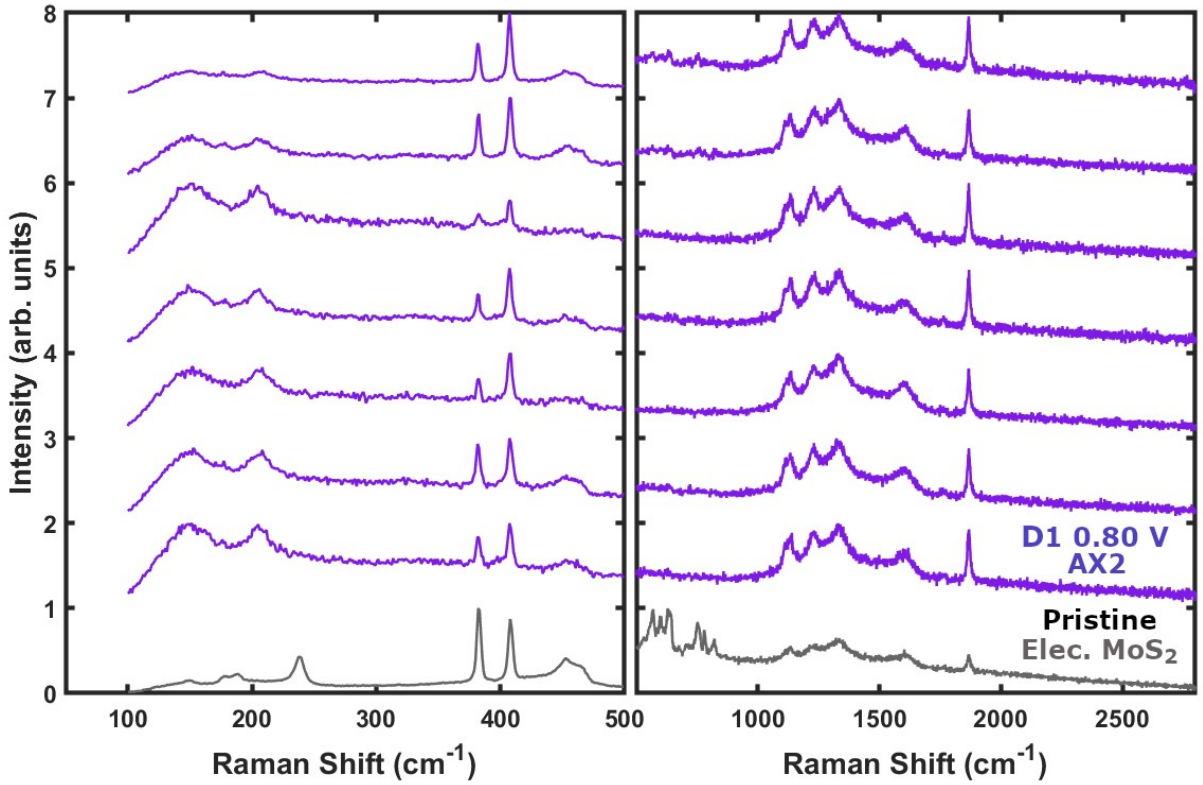

Figure SI 25. Ex situ air-free Raman spectroscopy (785 nm) of **D1 0.80 V** (~ 36 µm) electrode segment **AX2**. Multiple locations scanned across the electrode for MoS_2 phase consistency.

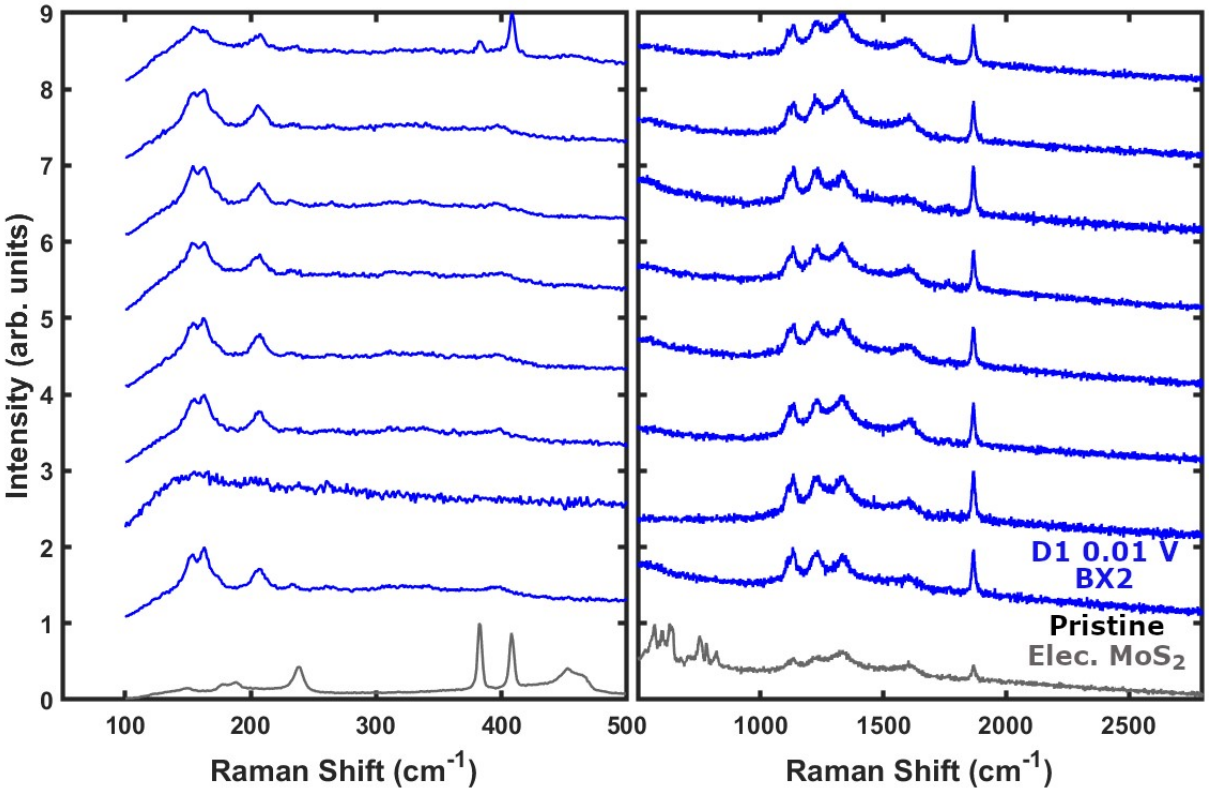

Figure SI 26. Ex situ air-free Raman spectroscopy (785 nm) of **D1 0.01 V** (~ 36 µm) electrode segment **BX2**. Multiple locations scanned across the electrode for MoS_2 phase consistency.

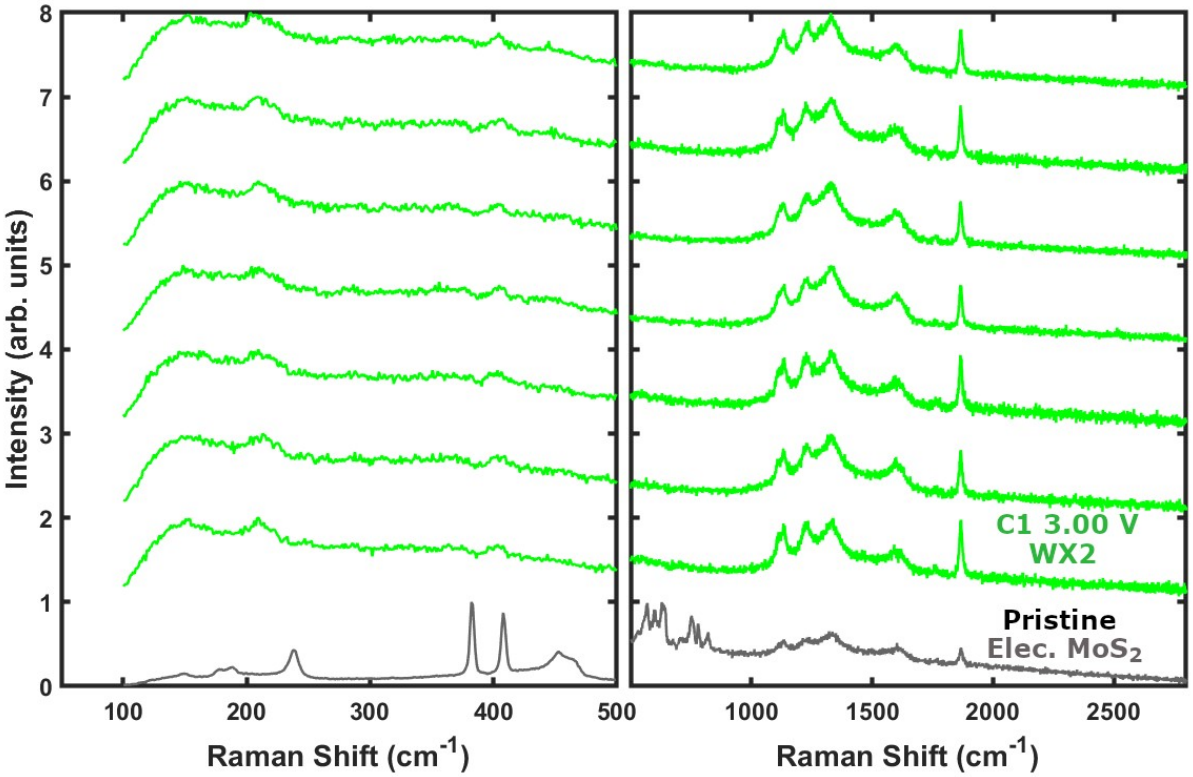

Figure SI 27. Ex situ air-free Raman spectroscopy (785 nm) of **C1 3.00 V** (~ 36 µm) electrode segment **WX2**. Multiple locations scanned across the electrode for MoS_2 phase consistency.

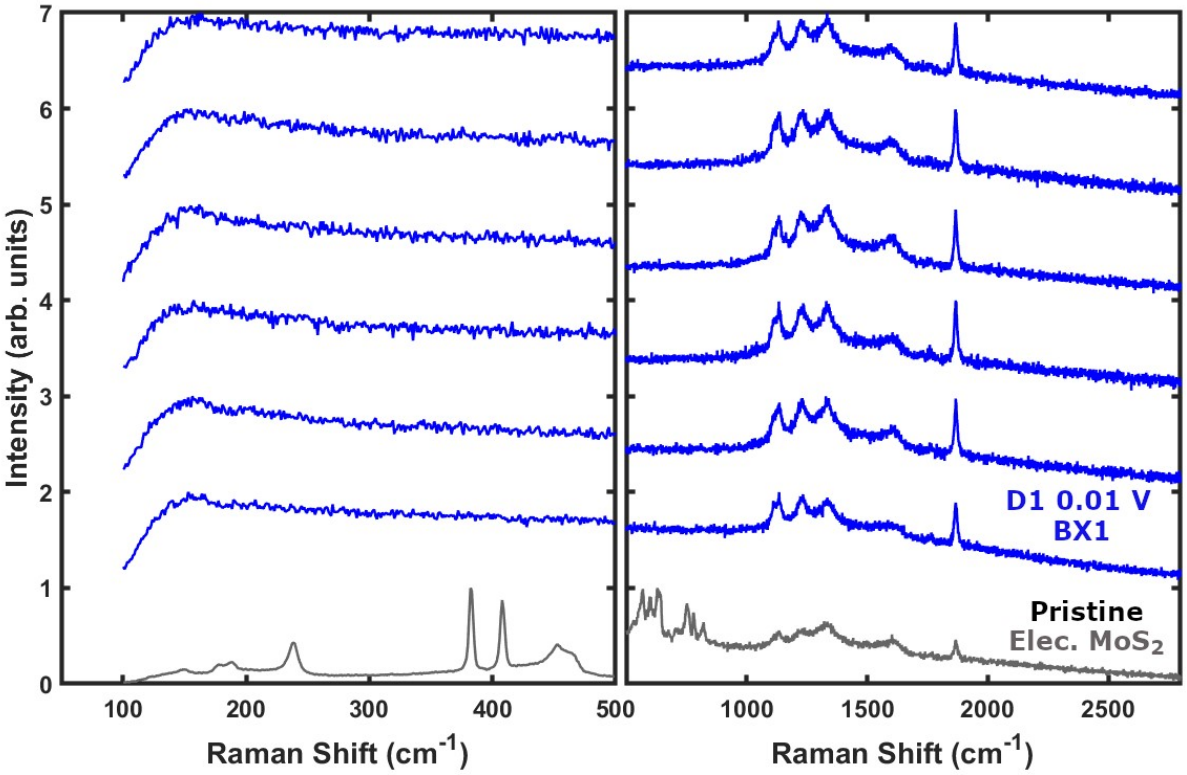

Figure SI 28. Ex situ air-free Raman spectroscopy (785 nm) of **D1 0.01 V** (~ 36 µm) electrode segment **BX1**. Multiple locations scanned across the electrode for MoS_2 phase consistency.

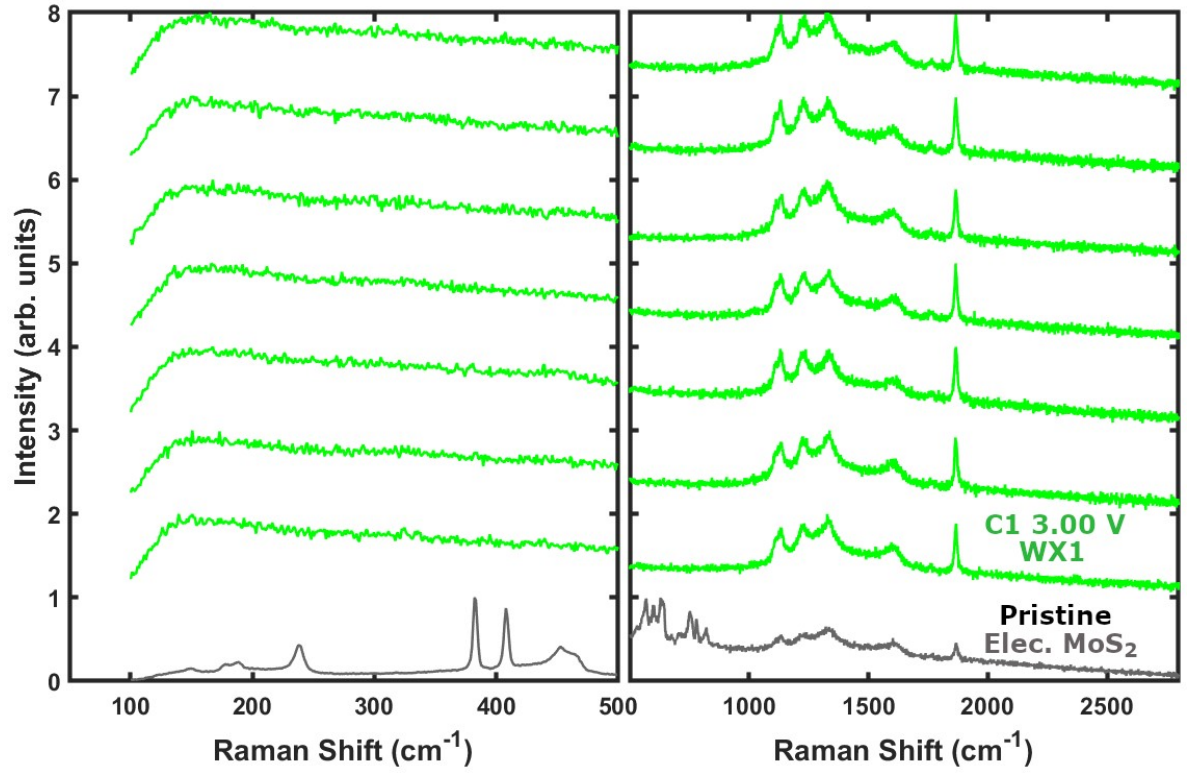

Figure SI 29. Ex situ air-free Raman spectroscopy (785 nm) of **C1 3.00 V** (~ 36 µm) electrode segment **WX1**. Multiple locations scanned across the electrode for MoS_2 phase consistency.

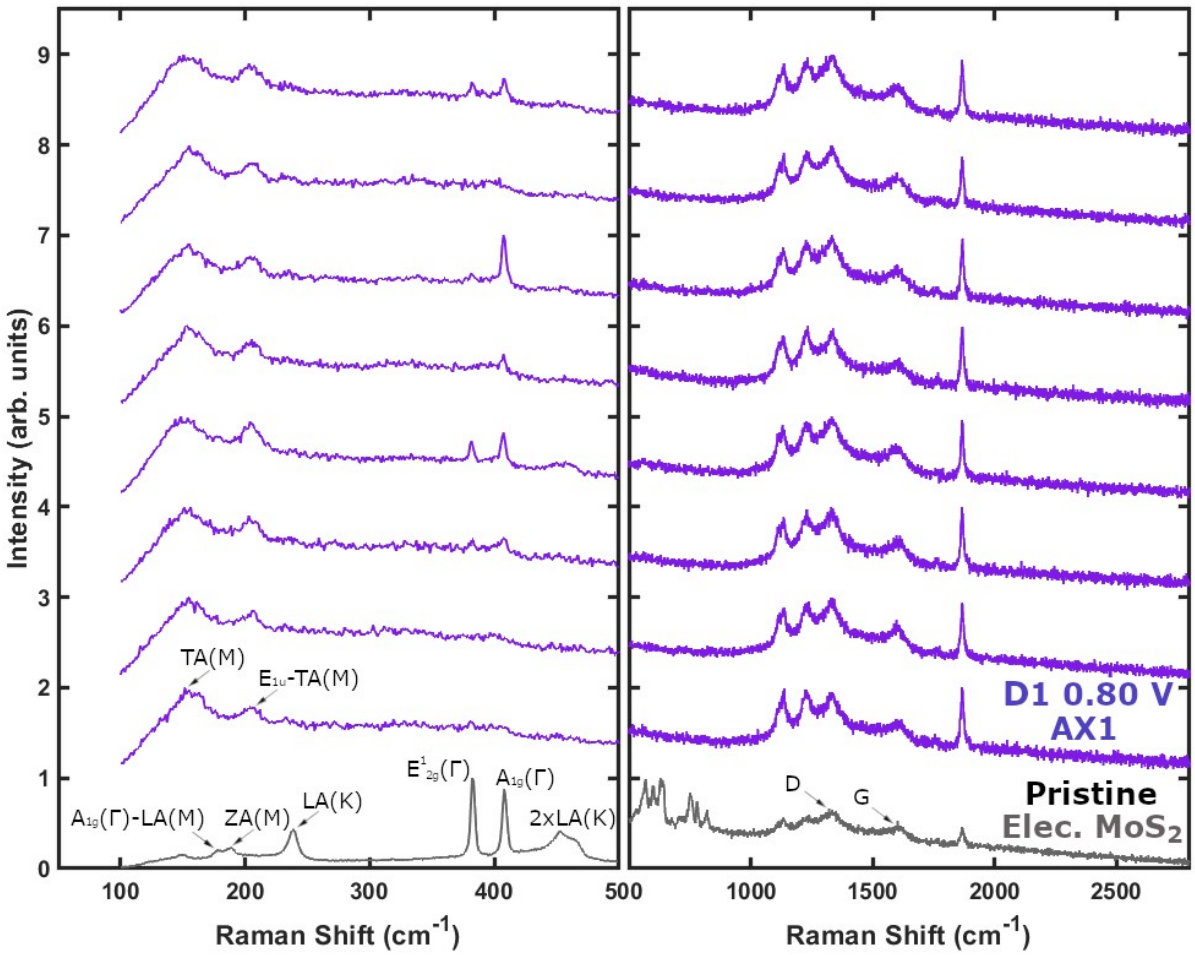

Figure SI 30. Ex situ air-free Raman spectroscopy (785 nm) of **D1 0.80 V** (~ 36 µm) electrode segment **AX1**. Multiple locations scanned across the electrode for MoS_2 phase consistency.

Ex situ Electrode XPS Analysis

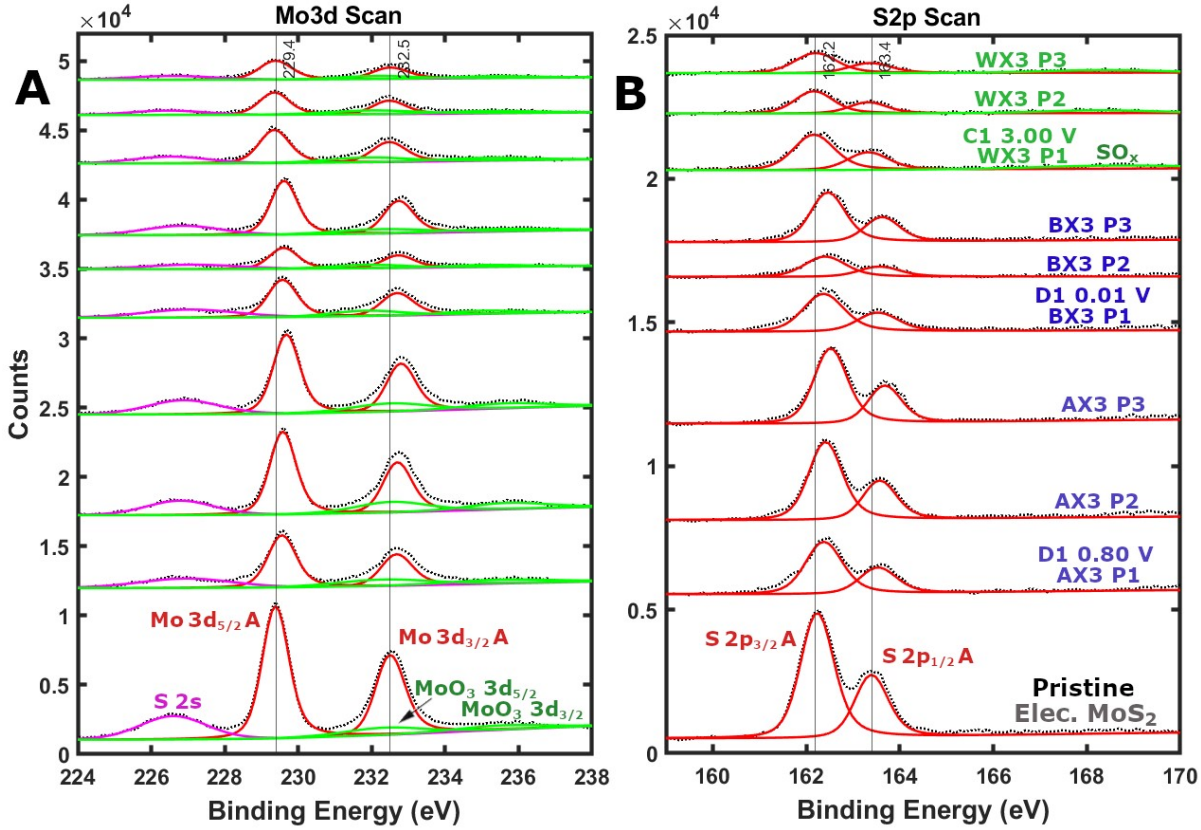

Figure SI 31. Ex situ air-free XPS of the **electrode centres** of ~ 36 µm thick MoS_2 electrodes cycled to **D1 0.80 V** (**AX3**), **D1 0.01 V** (**BX3**), and **C1 3.00 V** (**WX3**) in a lithium-metal half-cell at a current density of 200 mA/g. (A) Mo 3d region and (B) S 2p region.

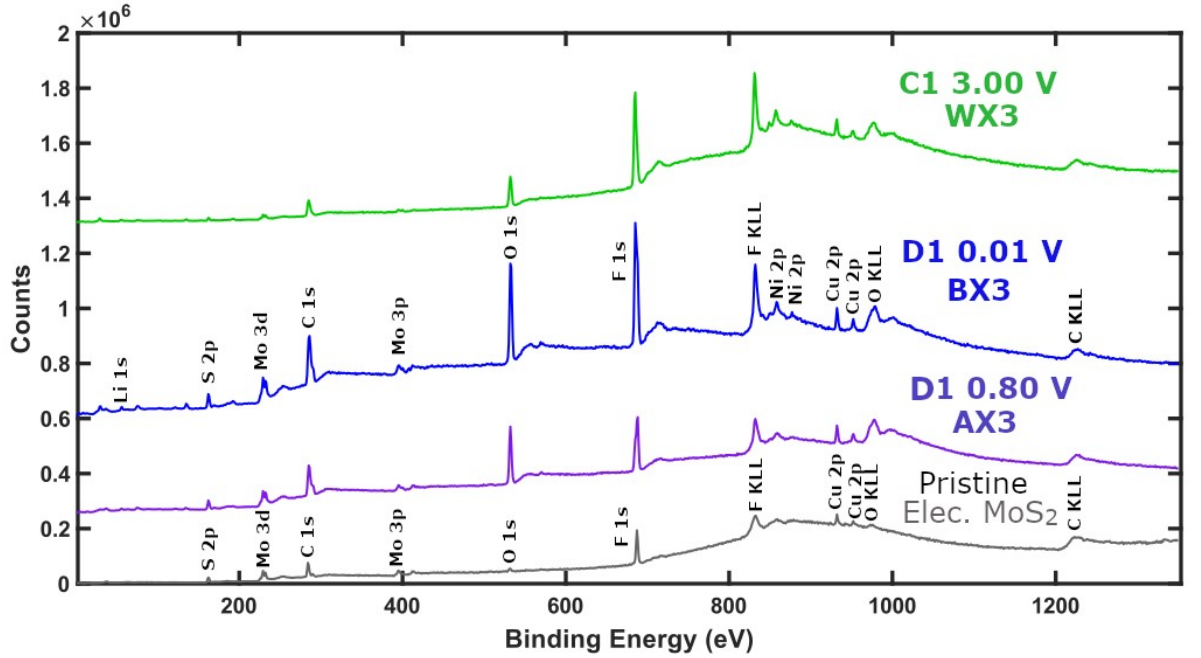

Figure SI 32. Ex situ air-free XPS of the **electrode centres** of ~ 36 µm thick MoS_2 electrodes cycled to **D1 0.80 V** (**AX3**), **D1 0.01 V** (**BX3**), and **C1 3.00 V** (**WX3**) in a lithium-metal half-cell at a current density of 200 mA/g.

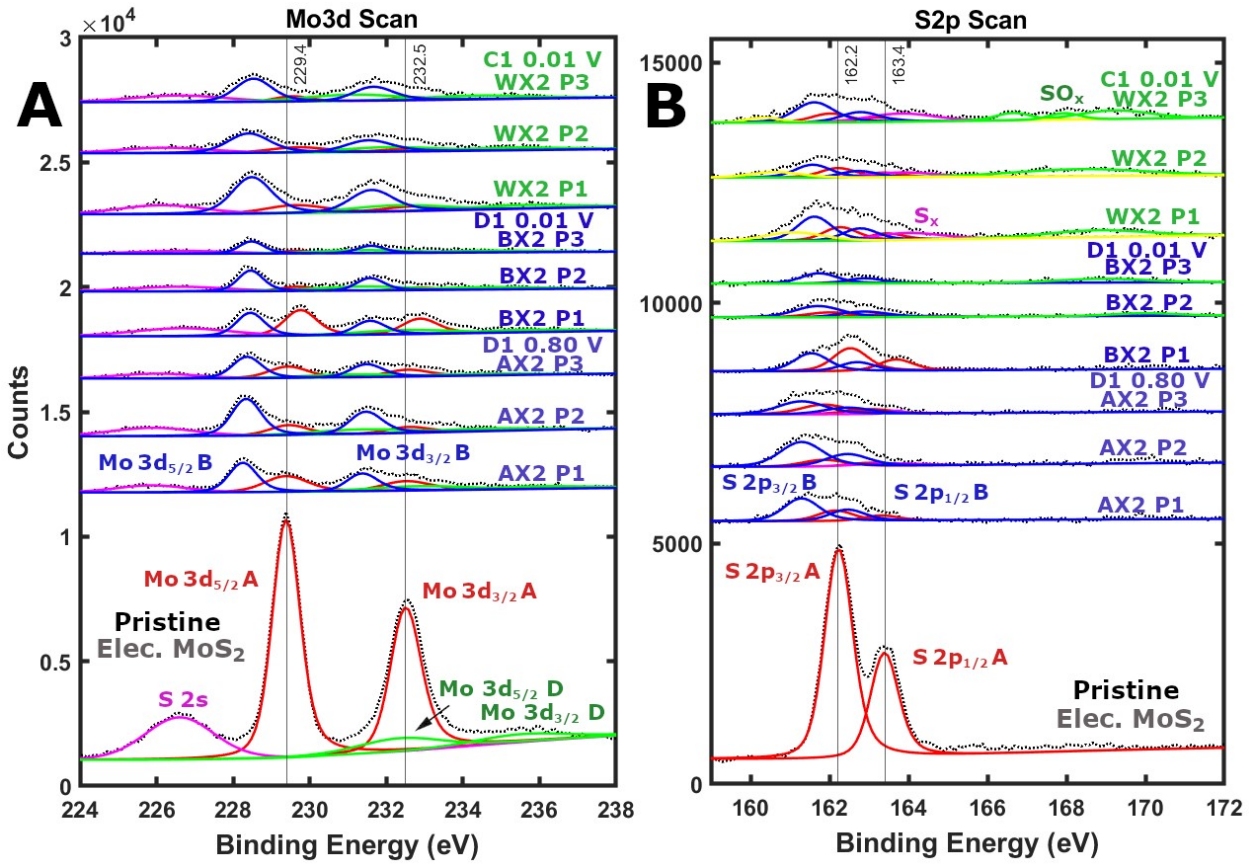

Figure SI 33. Ex situ air-free XPS of the **middle electrode rings** of ~ 36 µm thick MoS_2 electrodes cycled to **D1 0.80 V** (**AX2**), **D1 0.01 V** (**BX2**), and **C1 3.00 V** (**WX2**) in a lithium-metal half-cell at a current density of 200 mA/g. (A) Mo 3d region and (B) S 2p region.

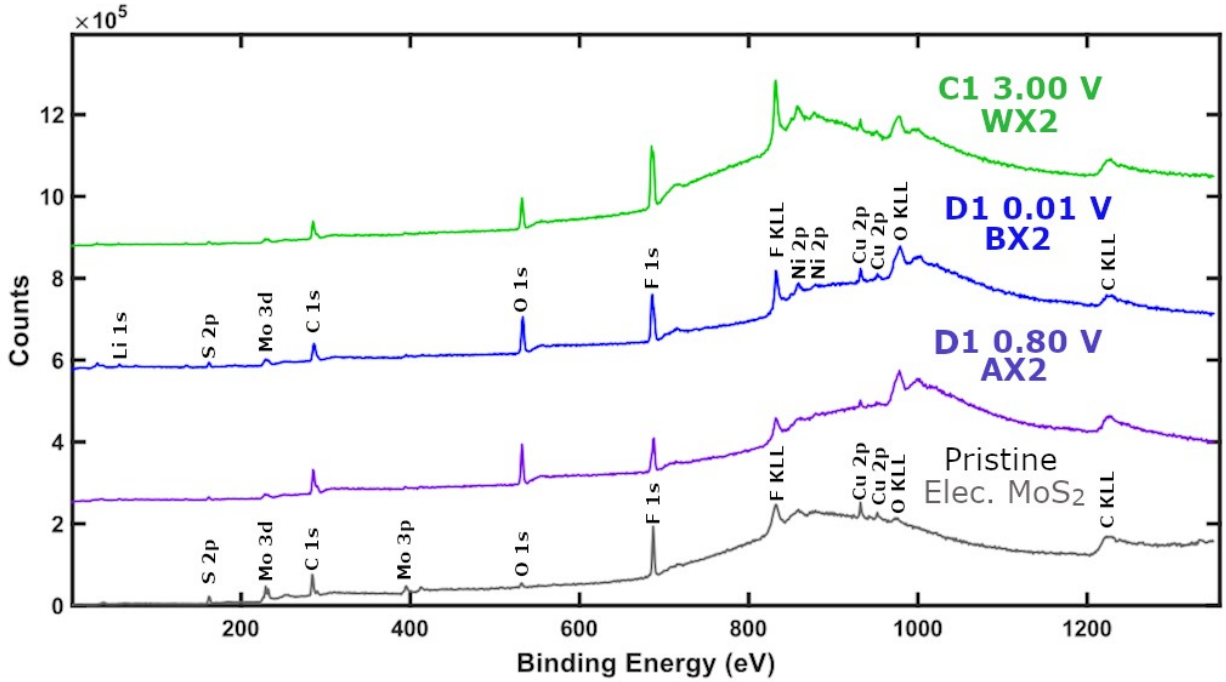

Figure SI 34. Ex situ air-free XPS survey scans of the **middle electrode rings** of ~ 36 µm thick MoS_2 electrodes cycled to **D1 0.80 V**, **D1 0.01 V**, and **C1 3.00 V** in a lithium-metal half-cell at a current density of 200 mA/g.

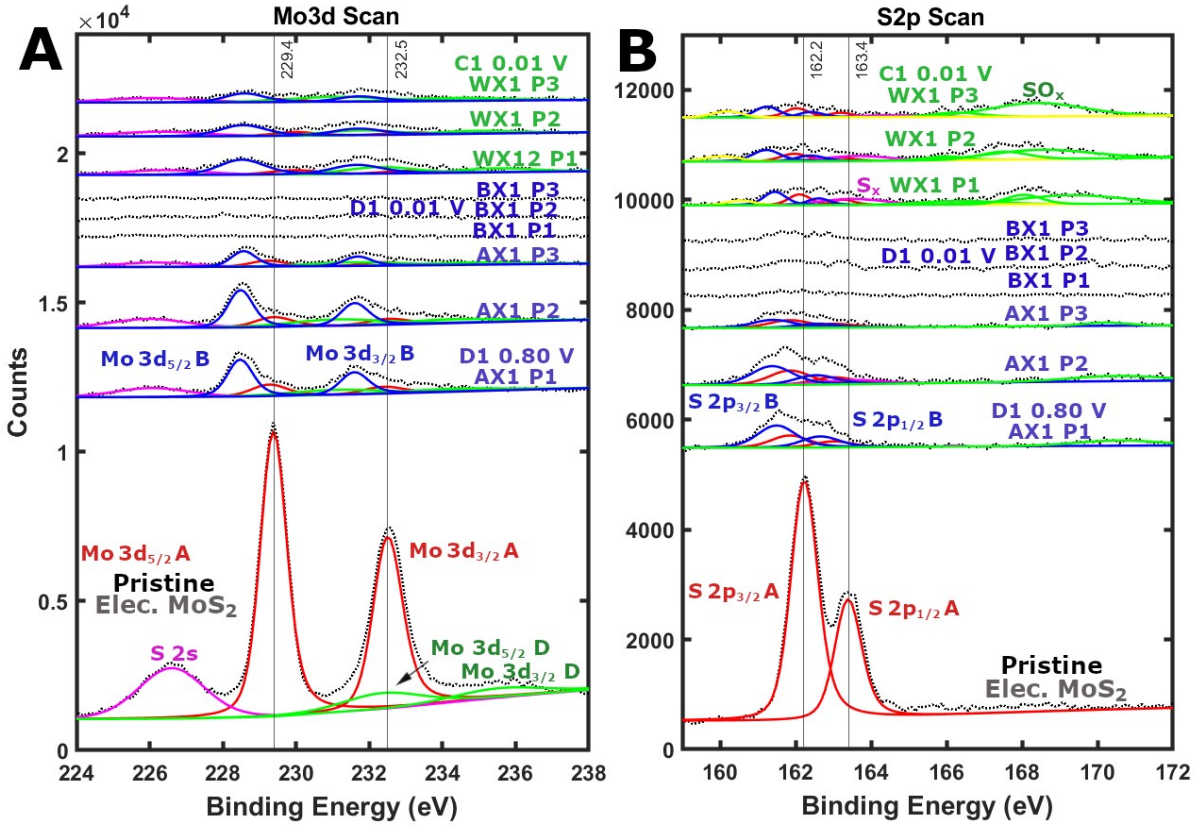

Figure SI 35. Ex situ air-free XPS of the **outer electrode rings** of ~ 36 µm thick MoS_2 electrodes cycled to **D1 0.80 V** (**AX1**), **D1 0.01 V** (**BX1**), and **C1 3.00 V** (**WX1**) in a lithium-metal half-cell at a current density of 200 mA/g. (A) Mo 3d region and (B) S 2p region.

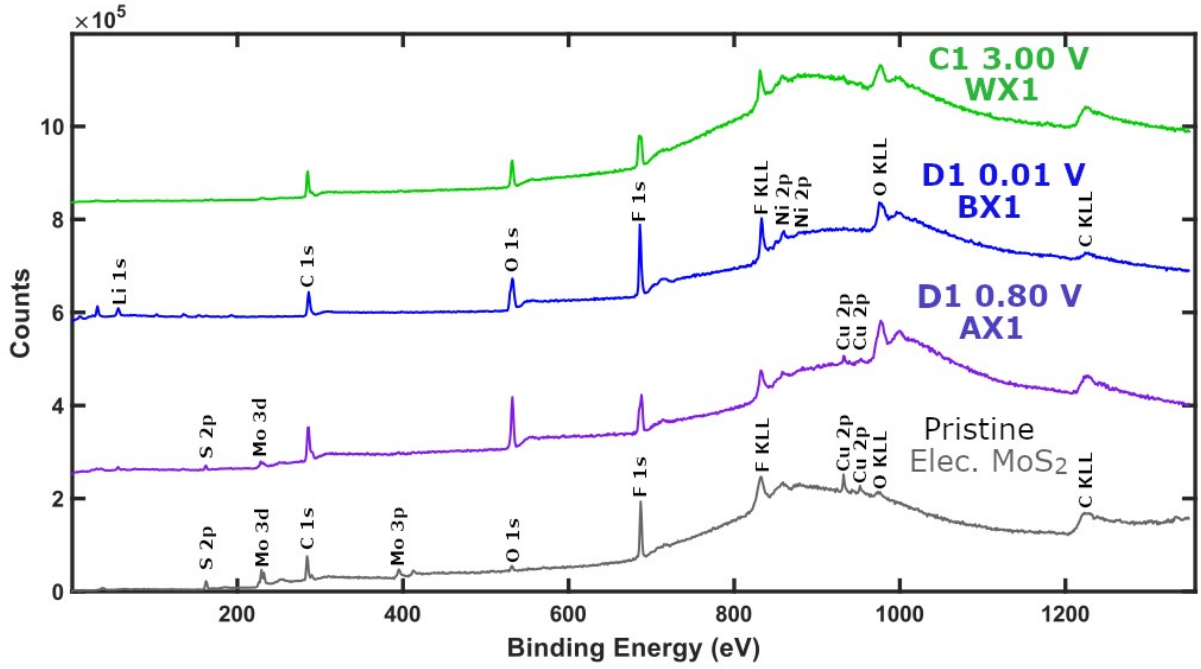

Figure SI 36. Ex situ air-free XPS of the **outer electrode rings** of ~ 36 µm thick MoS_2 electrodes cycled to **D1 0.80 V** (**AX1**), **D1 0.01 V** (**BX1**), and **C1 3.00 V** (**WX1**) in a lithium-metal half-cell at a current density of 200 mA/g.

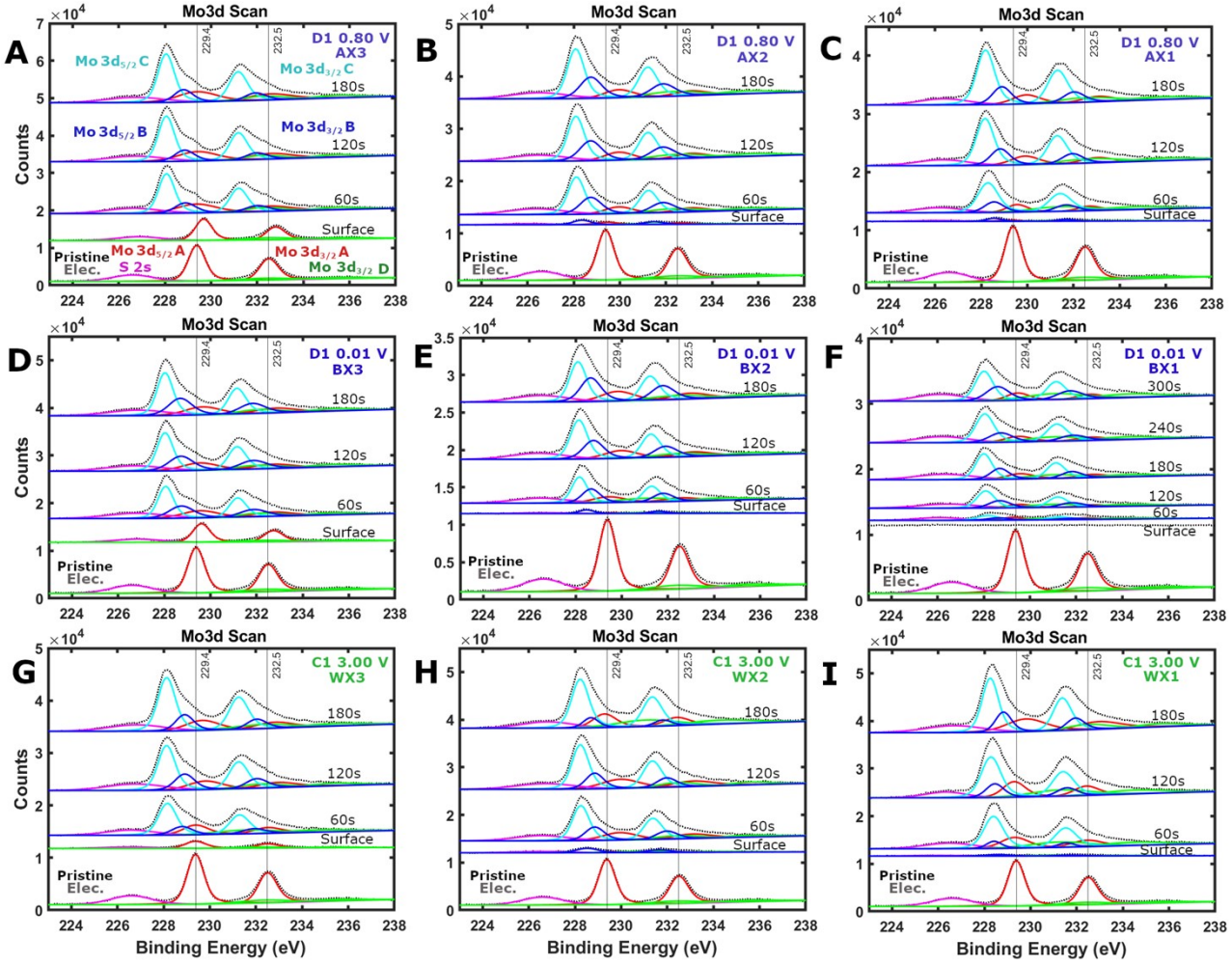

Figure SI 37. Ex situ air-free XPS of the Mo 3d region in the **electrode rings** of ~ 36 µm thick MoS_2 electrodes cycled to **D1 0.80 V** (A – C), **D1 0.01 V** (D – F), and **C1 3.00 V** (G – I) in a lithium-metal half-cell at a current density of 200 mA/g.

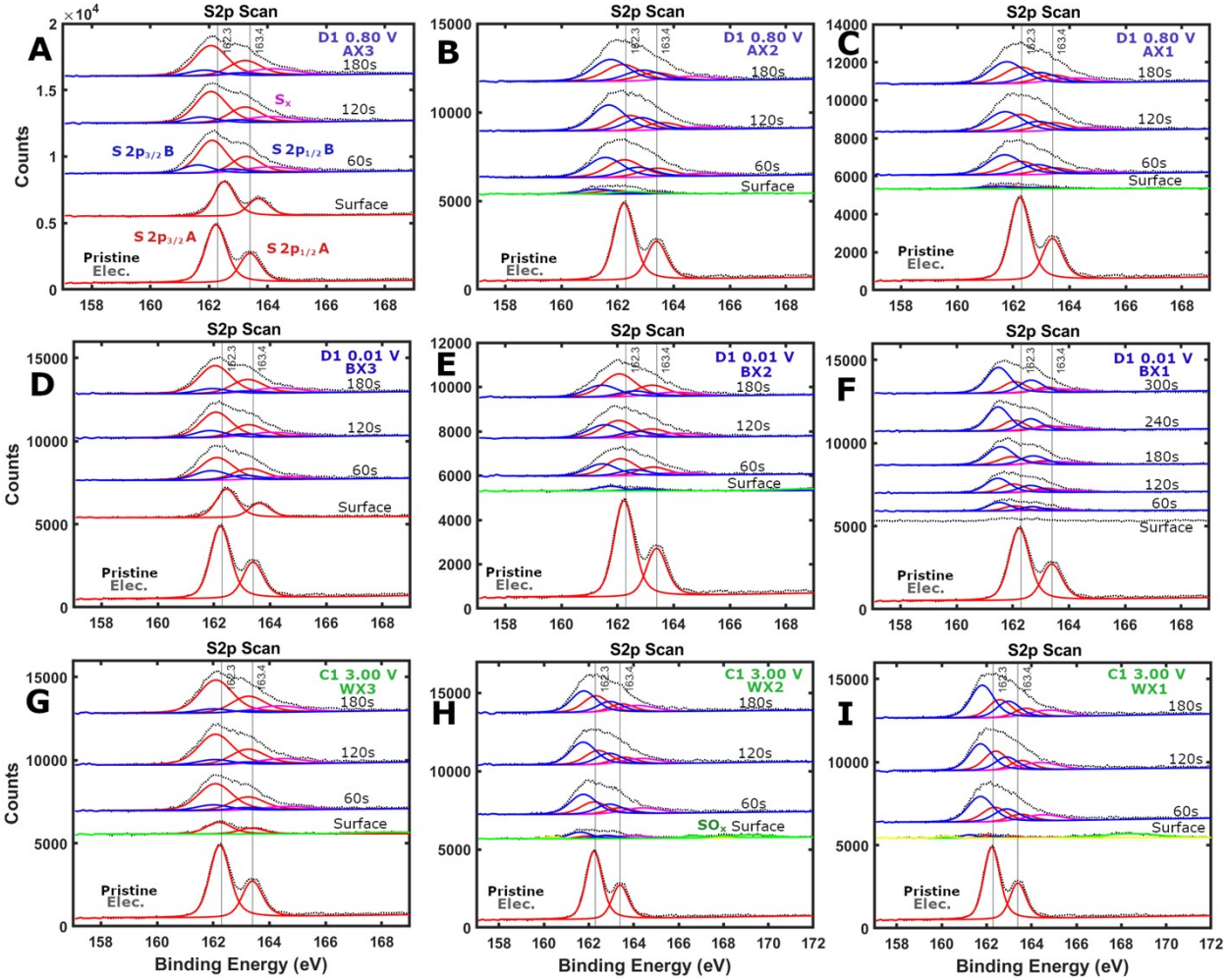

Figure SI 38. Ex situ air-free XPS of the S 2p region in the **electrode rings** of ~ 36 µm thick MoS_2 electrodes cycled to **D1 0.80 V** (A – C), **D1 0.01 V** (D – F), and **C1 3.00 V** (G – I) in a lithium-metal half-cell at a current density of 200 mA/g.

Note II: XPS Details of Mo 3d & S 2p Regions

Pristine MoS_2 powder and electrodes were dried at 60°C under vacuum for 24 hours prior to XPS analysis. On the other hand, cycled electrode segments were left to dry in an argon-filled glovebox (O_2, H_2O < 0.5 ppm), then taken directly from the glovebox to the XPS spectrometer vacuum antechamber using an air-free sample transfer holder.

Depth profiling was conducted with Ar^+ ions with an ion energy of 3,000 eV and a high ion current.

Fitting of all XPS scans presented in the study were carried out in CasaXPS. All regions utilise a U2 Tougard background.

For the Mo 3d region, four sets of Mo split orbital peak pairs (Mo $3d_{5/2}$ & $3d_{3/2}$) were considered, including 2H MoS_2 (~ 229.1 eV), 1T MoS_2 (~ 228.7 eV), MoS_{2-x} (~ 228.1 eV), and MoO_3 (~ 231.6 eV), as well as the S 2s peak (~ 224.6) eV. The peak positions are not fixed and the list provided is simply exemplary. Instead, for each peak pair the Mo $3d_{3/2}$ peak is restricted by a separation of + 3.1 eV, 66.7 % area, and 110 % FWHM relative to its major split peak couple Mo $3d_{5/2}$.

Similarly, for the S 2p region pairs of couplet peaks (S $2p_{3/2}$ & $2p_{1/2}$) are considered for the 2H MoS_2/MoS_{2-x} (~ 162.3 eV) and 1T MoS_2 (~ 161.9 eV) phases. Again, the positions are not fixed but serve as an example. The S^{2-} $2p_{1/2}$ peak is restricted by a separation of + 1.16 eV, 50 % area, and 100 % FWHM relative to its larger S^{2-} $2p_{3/2}$ peak couple. Additionally, elemental sulphur Sx (163 – 165 eV) and sulphates SOx (166 – 169 eV) are considered in certain regions.

In all cases, the Mo $3d_{5/2}$, Mo $3d_{3/2}$, S $2p_{3/2}$, and S $2p_{1/2}$ peaks are fit with asymmetric TA(1,1,300), TA(1,2,300), TA(1,1,300), and TA(1,1,300) line shapes, respectively. All additionally peaks utilise a LA(1.53,243) line shape.

All XPS regions are fit by using the inbuilt residual STD (standard deviation) minimisation Marquardt algorithm.

References:

1 X. Fang, C. Hua, X. Guo, Y. Hu, Z. Wang, X. Gao, F. Wu, J. Wang and L. Chen, *Electrochim Acta*, 2012, **81**, 155–160.

2 X. Fang, X. Guo, Y. Mao, C. Hua, L. Shen, Y. Hu, Z. Wang, F. Wu and L. Chen, *Chem Asian J*, 2012, **7**, 1013–1017.

3 L. Wang, Z. Xu, W. Wang and X. Bai, *J Am Chem Soc*, 2014, **136**, 6693–6697.

4 Z. Zhu, S. Xi, L. Miao, Y. Tang, Y. Zeng, H. Xia, Z. Lv, W. Zhang, X. Ge, H. Zhang, J. Wei, S. Cao, J. Chen, Y. Du and X. Chen, *Adv Funct Mater*, DOI:10.1002/adfm.201904843.

5 W. Choi, Y. S. Choi, H. Kim, J. Yoon, Y. Kwon, T. Kim, J. H. Ryu, J. H. Lee, W. Lee, J. Huh, J. M. Kim and W. S. Yoon, *Chemistry of Materials*, 2021, **33**, 1935–1945.

6 T. Liu, G. Melinte, O. Dolotko, M. Knapp and B. Mendoza-Sánchez, *Journal of Energy Chemistry*, 2022, **78**, 56–70.

7 L. Zhang, D. Sun, J. Kang, J. Feng, H. A. Bechtel, L. W. Wang, E. J. Cairns and J. Guo, *Nano Lett*, 2018, **18**, 1466–1475.

8 G. Wang, Y. Zhang, H. S. Cho, X. Zhao, F. Kim and J. Zou, *ACS Appl Energy Mater*, 2021, **4**, 14180–14190.